

DEMODULATION OF A MAGNETOSTRICTION-BASED  
FIBER INTERFEROMETER

by

Lauren Getz

Submitted in partial fulfillment of the  
requirements for Departmental Honors in  
the Department of Engineering  
Texas Christian University  
Fort Worth, Texas

May 8, 2017

DEMODULATION OF A MAGNETOSTRICTION-BASED  
FIBER INTERFEROMETER

Project Approved:

Supervising Professor: Tristan Tayag, Ph.D.

Department of Engineering

Stephen Weis, Ph.D.

Department of Engineering

Nalin Kumar, Ph.D.

UHV Technologies

## ABSTRACT

Magnetoencephalography, or MEG, is one particular technique of neuroimaging. It is a non-invasive and safe method of imaging the magnetic fields generated in the brain. There are currently a number of techniques developed for magnetic field sensing, including fiber-optic-based magnetic field sensors. Fiber optic sensors offer advantages due to their small size, low weight, and immunity to electromagnetic interference. This paper explains the current MEG neuroimaging system compared to alternative neuroimaging methods and addresses potential improvements using fiber optic sensors, such as magnetostrictive sensors. The advantages of these fiber-optic-based magnetic sensors over alternative magnetic field sensing techniques are explored. An experimental system is described, and a demodulation algorithm for the system is outlined. Finally, a theoretical analysis using magnetostrictive materials for MEG application is developed.

## TABLE OF CONTENTS

|   |           |
|---|-----------|
| <b>SECTION 1: MAGNETOENCEPHALOGRAPHY</b> .....  | <b>5</b>  |
| 1.1 INTRODUCTION.....   | 5         |
| 1.2 BIOMAGNETISM.....   | 5         |
| 1.3 MAGNETOENCEPHALOGRAPHY (MEG).....   | 7         |
| 1.4 OTHER METHODS OF NEUROIMAGING .....   | 11        |
| 1.5 APPLICATIONS AND ADVANCES .....   | 15        |
| 1.6 CONCLUSION.....   | 16        |
| <b>SECTION 2: FIBER-OPTIC-BASED MAGNETIC FIELD SENSORS</b> .....                      | <b>17</b> |
| 2.1 INTRODUCTION.....   | 17        |
| 2.2 MAGNETOSTRICTION SENSORS .....  | 17        |
| 2.3 OPTIMIZING THE MAGNETIC FIELD DETECTION SENSITIVITY .....                         | 21        |
| 2.4 MAGNETOSTRICTIVE MATERIALS .....  | 22        |
| 2.5 FARADAY EFFECT SENSORS .....  | 24        |
| 2.6 LORENTZ FORCE SENSORS .....   | 27        |
| 2.7 ADVANTAGES OF FIBER OPTIC SENSORS OVER SQUID.....                                 | 28        |
| 2.8 CONCLUSION .....  | 29        |
| <b>SECTION 3: EXPERIMENTAL SETUP</b> .....  | <b>30</b> |
| 3.1 INTRODUCTION.....   | 30        |
| 3.2 MACH-ZEHNDER INTERFEROMETER.....  | 30        |
| 3.3 EXPERIMENTAL SETUP .....  | 31        |
| 3.4 INTERFEROMETER SIGNAL .....   | 32        |
| 3.5 CONCLUSION.....   | 40        |
| <b>SECTION 4: ULTIMATE RESOLUTION OF AN INTERFEROMETRIC<br/>MAGNETIC SENSOR</b> ..... | <b>41</b> |
| 4.1 INTRODUCTION.....   | 41        |
| 4.2 THEORY AND ANALYSIS .....   | 41        |
| 4.3 METGLAS .....   | 45        |
| 4.4 TERFENOL-D.....   | 46        |
| 4.5 CONCLUSION .....  | 47        |
| <b>REFERENCES</b> .....   | <b>49</b> |
| <b>APPENDIX A: MAGNETIZATION ANISOTROPY FIELD</b> .....                               | <b>53</b> |
| REFERENCES .....  | 57        |
| <b>APPENDIX B</b> .....   | <b>58</b> |
| <b>APPENDIX C</b> .....   | <b>60</b> |

## SECTION 1: MAGNETOENCEPHELOGRAPHY

### 1.1 Introduction

The human brain is one of the most complex and intricately organized biological structures and has been studied by researchers for decades. Attempts at understanding the human brain have led to numerous methods of brain testing and brain imaging. Magnetoencephalography is one such method of neuroimaging. This method utilizes the magnetic fields naturally generated in the brain to map brain function. The magnetic fields generated in the human body are often studied in order to gain insight about normal physiology and to develop new techniques for medical diagnosis.

### 1.2 Biomagnetism

Biomagnetism is the phenomenon of magnetic fields produced by biological systems. The human body produces magnetic fields in two ways: by electric currents and by ferromagnetic particles. In the first method, electric currents naturally generated in the body by the motion of ions produce a magnetic field [1], [2]. Neurons, which are cells in the brain and nervous system, often send signals to each other and to the body's muscles and sensory organs. As these signals are being transmitted, muscles, nerves, and other organs generate currents of sodium, potassium, and chlorine ions. The heart and brain are two organs that generate ion currents that are often studied. In the heart, the same ion current produced by the heart muscle, which serves as the basis for the electrocardiogram, also generates a magnetic field around the chest. This magnetic field, when measured, is called a magnetocardiogram. The same is true for the brain. The

same ion current produced by the brain, which is the basis for the electroencephalogram, also generates a magnetic field over the head. This magnetic field, when measured, is called a magnetoencephalogram. The general process is shown in Figure 1.1, where the volume conductor is the general mass of fluids and tissues in the part of the body being measured. Blood in the body is electrically neutral, and thus the flow of blood establishes zero electrical current and produces no magnetic field.

The second method by which magnetic fields are produced involves magnetic materials in the human body, as described in Ref. [1]. Magnetic materials produce a magnetic field in response to an external magnetic field that has been applied to the material. The material can be ferromagnetic, paramagnetic, or diamagnetic. The human body contains all three of these substances, but the most common type of particle is ferromagnetic. These magnetic particles are insoluble contaminants in the body. The most prominent is magnetite,  $\text{Fe}_3\text{O}_4$ , which is found in the lungs and is harmless to the body.

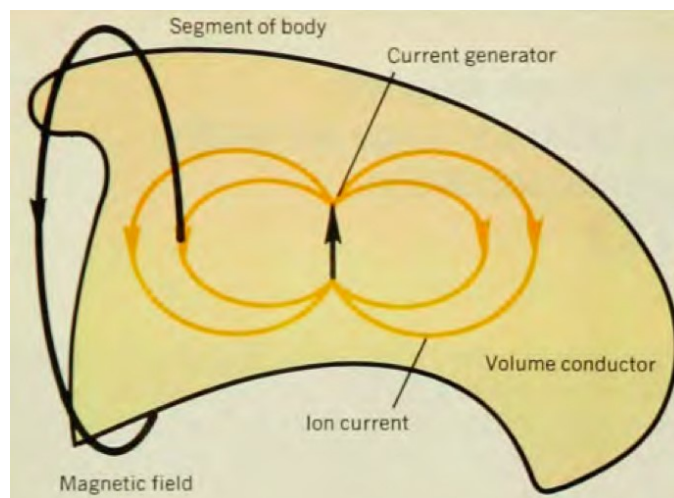


**Figure 3.1.1** The body produces magnetic fields by currents from muscles and nerves. A current dipole generates ion currents that result in a magnetic field [1].

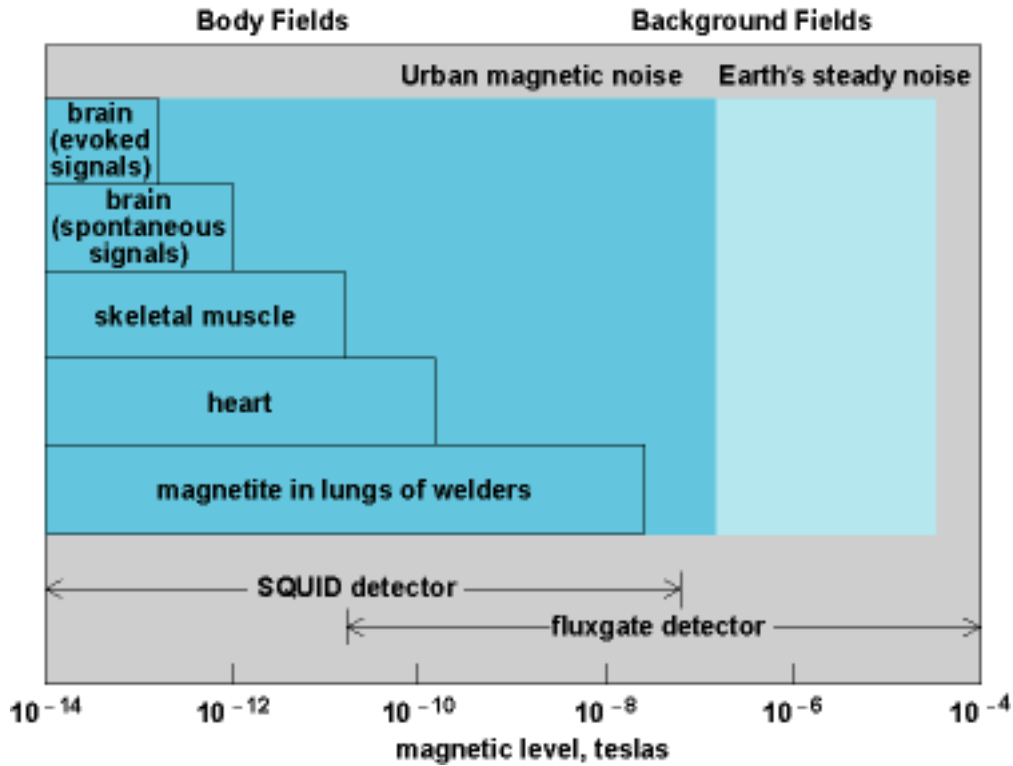


Figure 1.3.2 The levels of the magnetic fields around the body and in the background [3]

The strengths of these magnetic fields are very weak. As shown in Figure 1.2, they typically range from  $10^{-14}$  to  $10^{-9}$  T. In comparison, the Earth's magnetic field is on the order of  $10^{-5}$  T. Because the magnetic fields in the body are so small, a special measuring technique, described in the following sections, has been developed that eliminates background noise that may contaminate the reading of the magnetic fields coming from the body. This noise comes from the magnetic fields of a variety of sources, from computers to cell phones to the Earth itself.

### 1.3 Magnetoencephalography (MEG)

Magnetoencephalography is a non-invasive method of imaging the magnetic fields generated in the brain. A detector for measuring the body's fields was developed

by James Zimmerman [1]. As described in Ref. [4], the magnetic fields generated by the currents from neurons induce an electric current within a detection coil. Coupled to this coil is a superconducting quantum interference device, or SQUID. As explained in Ref. [5], the SQUID sensor is based on the interactions observed between the electric current generated in the detector and the magnetic field to be sensed. The superconductor of the SQUID sensors requires the sensors to be cooled below a superconducting transition temperature. At this superconducting temperature, the materials have very low resistance to the flow of current. Figure 1.3 shows the schematic of a SQUID sensor.

When a time-changing magnetic flux flows through a ring comprised of superconducting material, such as that shown in Figure 1.4, a current will be induced in the ring. As described in Ref. [5], Brian David Josephson predicted that supercurrent, which is an electric current that flows without dissipation, could flow between two superconductors separated by a thin layer of insulation. The magnitude of this supercurrent through the “Josephson junction” is affected by the presence of a magnetic

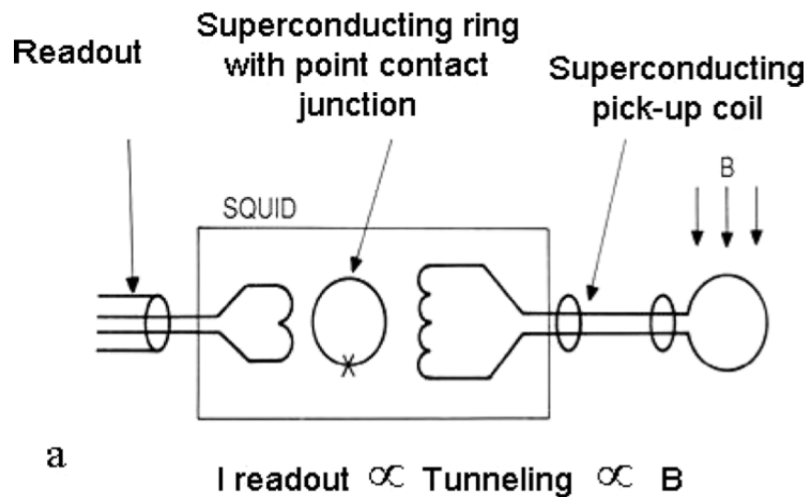


**Figure 1.3** A schematic of a SQUID sensor [5]

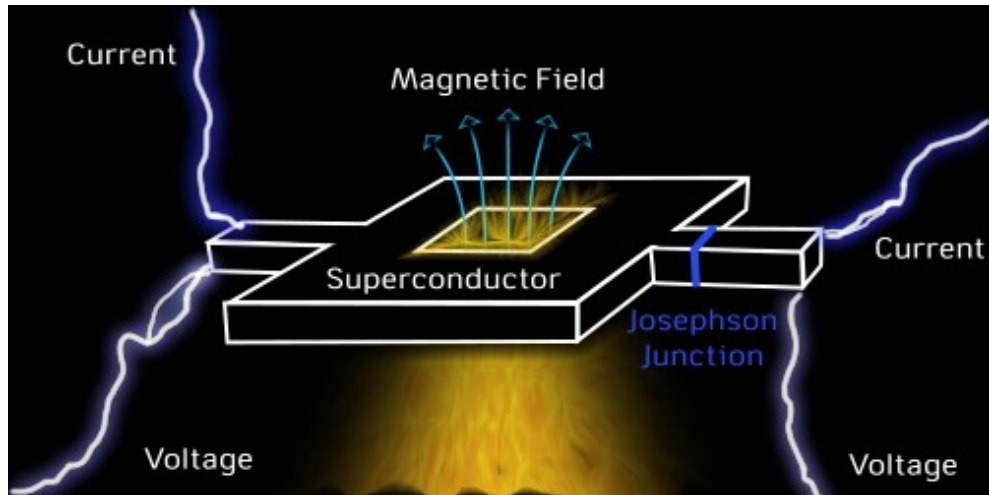


**Figure 1.4** A schematic of a SQUID sensor [6]

field. This forms the basis for the SQUID sensor. Figure 1.4 shows a diagram of a Josephson junction, where an insulator separates two superconductors. Josephson showed that this supercurrent would be an oscillating function of the magnetic field intensity in this Josephson junction. In a SQUID sensor, the periodic variations in the current are used to measure the current in the superconducting ring, and consequently, the magnetic field. The superconducting ring is usually coupled inductively to a radio-frequency (RF) circuit, which provides a known bias field and acts as the output of the detector. Changes in the current in the ring result in a change in the resonant frequency of the circuit, causing the output signal to change periodically as the field varies. These changes in the field can be measured by counting the peaks and valleys, similar to counting fringes in an interference pattern of light.

The SQUID device itself is usually small. The superconducting ring used in a SQUID is generally a small toroid, only a few millimeters in diameter, and is made of a metal such as niobium or lead. As previously mentioned, in order to create superconducting conditions, the SQUID sensors must be kept at superconducting

temperatures. This low temperature is achieved by surrounding the sensors in liquid helium at 4.2 K, or  $-270^{\circ}\text{C}$ , and enclosing the entire apparatus within an insulated dewar, as shown in Figure 1.5. This results in a rather large and bulky machine, shown in Figure 1.6.

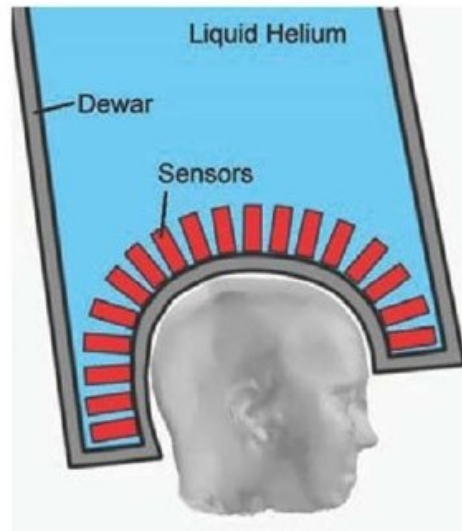


**Figure 1.5** The inside of a Magnetoencephalography system [7]

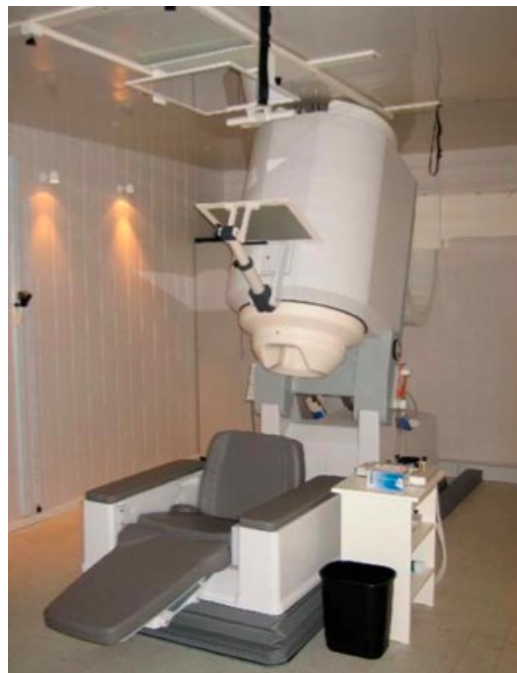


**Figure 1.6** A Magnetoencephalography system [4]

In recent MEG systems, hundreds of SQUID sensors are placed in the dewar's helmet, allowing the whole brain to be covered. The entire system, shown in Figure 1.6, is contained in a magnetically shielded room to avoid interference by external magnetic fields. SQUID systems can measure down to  $10^{-15}$  T at a frequency range of dc to 20 kHz [2]. According to Ref. [8], neuromagnetism generally involves frequencies below 100 Hz. So, MEG with SQUID systems is one neuroimaging technique that uses magnetic fields generated in the brain to map brain activity.

#### 1.4 Other Methods of Neuroimaging

In addition to MEG, there are a number of other neuroimaging techniques currently being used in the medical field. Electroencephalography (EEG) measures the electrical activity of the brain from electrodes placed on the head. The resulting traces, called an electroencephalogram, represent an electrical signal from a large number of neurons firing. An example of the equipment and readings is shown in Figure 1.7. Both MEG and EEG are completely non-invasive. As explained in Ref. [8], in both EEG and MEG, the measured field signals are generated by the same activity in the brain.

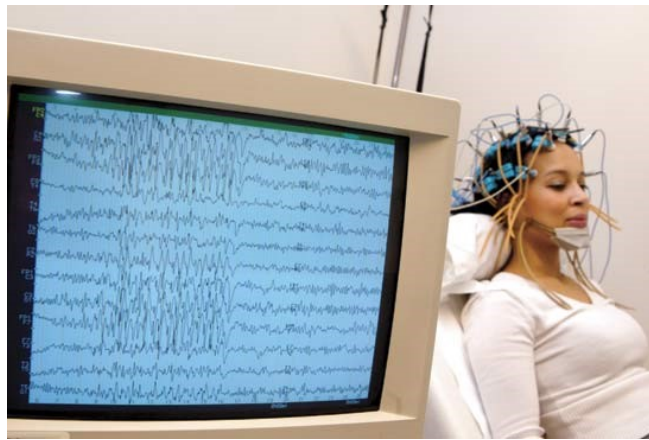


**Figure 1.7** A woman undergoing electroencephalography [12]

Two alternative major neuroimaging methods rely on changes in blood flow or blood oxygenation rather than electromagnetism. The first method, functional magnetic resonance imaging (fMRI) measures brain activity by detecting changes in blood flow and blood oxygenation occurring in response to neural activity. When a brain area is more active, it consumes more oxygen, causing increased blood flow in that area. This technique is used to generate activation maps that outline which parts of the brain are involved in a specific mental process. An fMRI machine is shown in Figure 1.8, and an example of a brain scan using this technique is shown in Figure 1.9.

The second method, positron emission tomography, or PET, maps functional processes in the brain by using trace amounts of a short-lived radioactive material, called a tracer. Because of this tracer's similarity to naturally occurring glucose, neurons take the tracer into their system but are not able to metabolize it. This phenomenon results in the tracer accumulating in active regions of the brain. As the radioactive material undergoes decay, positrons are emitted and sensed by a detector. Thus, areas with high radioactivity are associated with brain activity. A PET machine is shown in Figure 1.10, and an example of a PET brain scan is shown in Figure 1.11.



**Figure 1.8** An fMRI machine [12]

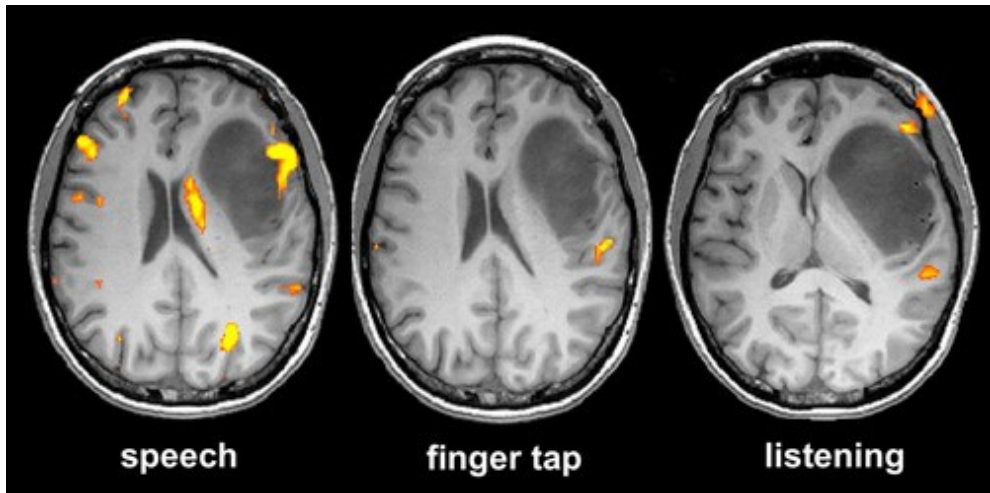


**Figure 1.9** Three fMRI scans showing different areas of the brain lighting up when certain tasks are performed [13]

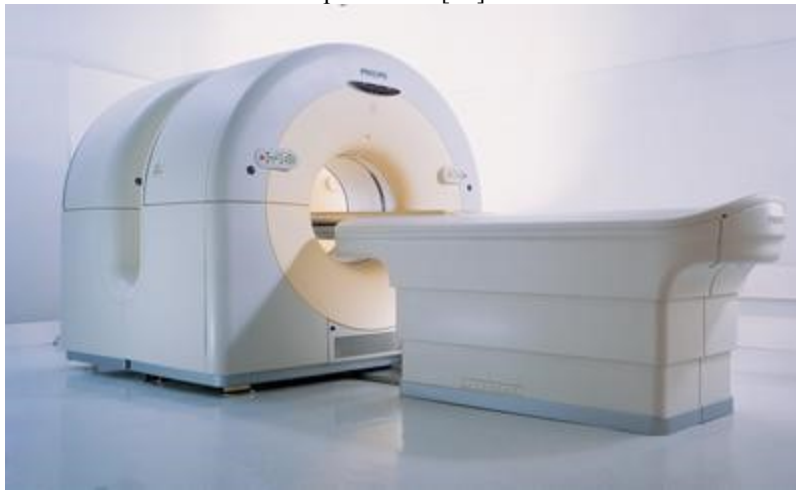


**Figure 1.10** A PET machine [14]

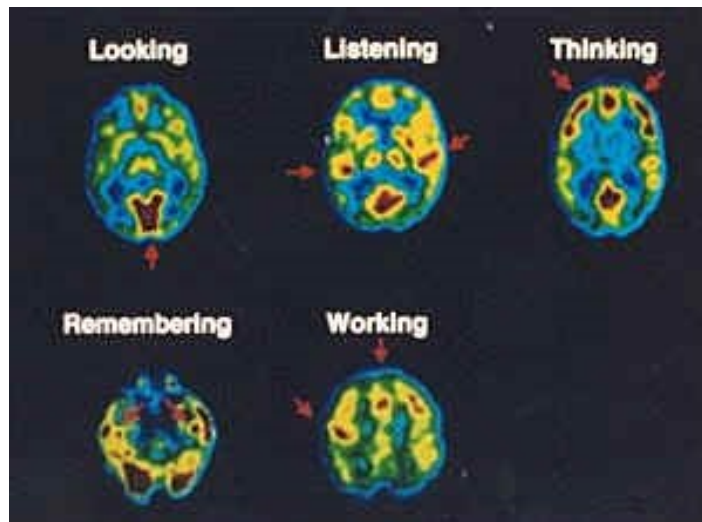


**Figure 1.11** Various PET scans showing brain activity associated with certain actions [15]

| Table 1.1 Methods of Neuroimaging |                     |                    |
|-----------------------------------|---------------------|--------------------|
|                                   | Temporal Resolution | Spatial Resolution |
| MEG [8], [9]                      | milliseconds        | centimeters        |
| EEG [8], [9]                      | milliseconds        | centimeters        |
| fMRI [9], [10]                    | deciseconds         | millimeters        |
| PET [9], [10]                     | minutes             | millimeters        |

The temporal and spatial resolutions for these techniques are shown in Table 1.1. Because the sensors used in MEG and EEG are in close proximity to the brain, both MEG and EEG are able to have high temporal resolutions on the order of milliseconds. However, the spatial resolutions of both EEG and MEG are not quite as high as other techniques and are on the order of centimeters. According to Ref. [9], this spatial resolution can vary depending on the nature of the particular neuronal activity being measured. Because both fMRI and PET depend on blood flow or blood oxygenation, they produce indirect correlations of the neuronal activity. Consequently, their readings are delayed, as shown by the lower temporal resolutions in Table 1.1. These low temporal resolutions express the fact that these techniques can only take pictures every few seconds or minutes. According to Ref. [9], fMRI has a relatively high spatial resolution on the order of millimeters and PET has a spatial resolution that falls between that of fMRI and EEG/MEG.

While each of the above techniques is used to create images of the brain, each method may be used for different functions. For example, although fMRI does not have as high of a temporal resolution as MEG, fMRI directly creates an image of the brain whereas MEG simply measures the activity of the brain. However, as noted in Ref. [8], once the brain's activity has been measured using MEG, the MEG scans are often combined with fMRI scans to view both together. Combining MEG measurements with

the anatomical images of the fMRI, known as sensor fusion, can lead to greater understanding of brain structure and function.

### 1.5 Applications and Advances

MEG has many potential applications, both clinically and in the research field. In addition to helping researchers learn more about the functions of parts of the brain, it allows doctors to develop improved treatment plans for patients suffering from a neurological disorder or from a traumatic brain injury. MEG has been used in patients with epilepsy, Alzheimer's disease, schizophrenia, and autism, as noted in Ref. [4]. MEG technology also allows those patients to receive an accurate and sensitive evaluation of their brain, without having to undergo an invasive method of testing.

Despite the advantages and usefulness of MEG, one major problem still remains: the large size of the measuring device. Currently, researchers are striving to develop alternative sensors to the widely used SQUID. One such device measures magnetic field signals with a chip-scale atomic magnetometer, or CSAM, based on the optical spectroscopy of alkali atoms, as described in Ref. [16]. These CSAMs provide a reduced sensitive volume and allow for possible low-cost manufacturing. However, their current design yields a lower fundamental sensitivity than the current SQUID sensor design. Research projects such as this show the continued efforts to improve neuroimaging and specifically MEG.

## 1.6 Conclusion

Of the many methods of investigating the structure and function of the brain, MEG technology offers a useful non-invasive method. Despite the massive size of SQUID-based MEG systems, it does produce temporal resolution on the order of milliseconds and spatial resolution on the order of centimeters. In addition to the SQUID sensors currently used in MEG systems, other magnetic sensors have the potential to be used for this application. One such magnetic sensor is a fiber-optic-based sensor, which is discussed in the next section. With its many applications in the health and research fields, MEG promises to lead to new insights in the quest for understanding the human brain.

## SECTION 2: FIBER-OPTIC-BASED MAGNETIC FIELD SENSORS

### 2.1 Introduction

Magnetic sensors are often used in many fields of scientific study, from research to military to medicine. Techniques developed for magnetic field sensors include search coils, fluxgates, superconducting quantum interference devices (SQUIDs), and fiber-optic-based sensors [17]. Fiber-optic-based magnetic field sensors offer advantages over other techniques due to their small size, low weight, and immunity to electromagnetic interference. There are numerous types of these sensors, including magnetostrictive sensors, Faraday effect sensors, and Lorentz force sensors.

### 2.2 Magnetostriction Sensors

Magnetostriction is a property of ferromagnetic materials that causes a dimensional change in the material when it is placed in a magnetic field. Magnetostrictive materials include Terfenol-D, Metglas, and nickel. This magnetostrictive material is attached to the fiber, traditionally either as a magnetostrictive jacket or as a bulk magnetostrictive element around which the optical fiber is wound [18]. When placed in a magnetic field, the magnetostrictive material changes shape. The material changes dimensions in every direction, but typically only the longitudinal change is studied, particularly in sensors [19]. The length change in the material causes a strain in the material and a change in the length of the fiber.

The change in the fiber's length can be detected using an interferometer, such as the Mach-Zehnder interferometer, shown in Figure 2.1, in which one arm of the interferometer consists of a magnetostrictive material bonded to the fiber. The magnetic

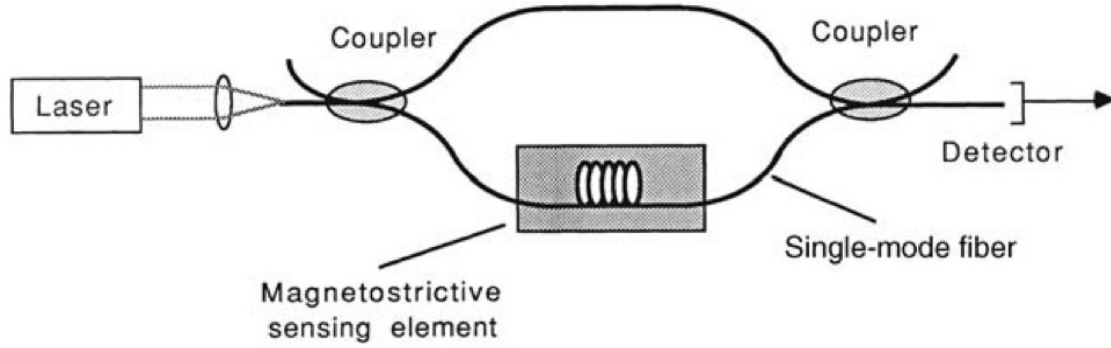


**Figure 2.1** Mach-Zehnder interferometer schematic with a magnetostrictive fiber optic magnetometer [20]

field-dependent phase shift  $\phi(H)$  induced in the interferometer is given by

$$\phi(H) = \frac{2\pi n \xi}{\lambda} L \eta \epsilon(H), \quad (2.1)$$

where  $\epsilon$  is the strain of the material,  $H$  is the externally applied magnetic field,  $\lambda$  is the free-space wavelength of the laser source,  $n$  is the refractive index of the fiber core,  $L$  is the interaction length between the fiber and magnetostrictive material,  $\eta$  is the strain transfer efficiency, and  $\xi$  is the strain optic correction factor [20]. For a silica fiber,  $\xi$  is approximately 0.78 and  $n$  is 1.46. However, only a portion of the strain developed by the magnetostrictive element will be transferred to the core of the optical fiber due to the losses that occur in the interface between the fiber and the material. The exact amount of strain transferred depends on the type and thickness of the adhesive between the magnetostrictive material and the fiber, the type of fiber coating material, and the dither frequency. Dither frequency will be explained in a following section. It is difficult to precisely measure  $\eta$ , but typical measured values range from 0.3 to 0.9.

Most ferromagnetic materials, such as iron, nickel, and cobalt, exhibit a magnetic-field-induced strain or magnetostriction. The magnetostriction of many materials can be written as

$$\epsilon = CH^2, \quad (2.2)$$

where  $C$  is the magnetostrictive constant for the material and  $H$  is the magnetic field [20]. This equation describes the coherent rotation model, shown in Figure 2.2. This model assumes that, in the absence of an externally applied magnetic field, the magnetic moments in the material point in either the positive or negative direction in relation to the anisotropy field,  $H_A$ , which describes the directional dependence of the magnetic moments in anisotropic materials. (Appendix A describes the anisotropy field.) When an external magnetic field is applied, the magnetic moments rotate in the direction of the applied field. When this happens, the magnetization increases linearly with the applied field. In addition to this increasing magnetization, a change in length of the material in the direction of the applied field is quadratically related to the applied field, according to equation 2.2. The strain will increase as the magnitude of the applied magnetic field increases above that of the anisotropy field. As shown in Figure 2.3, the strain approaches the saturation magnetostriction,  $\lambda_s$ , which is the fractional change in length in a given direction as the magnetostrictive material changes from a randomly demagnetized state to a fully magnetically saturated state [21].

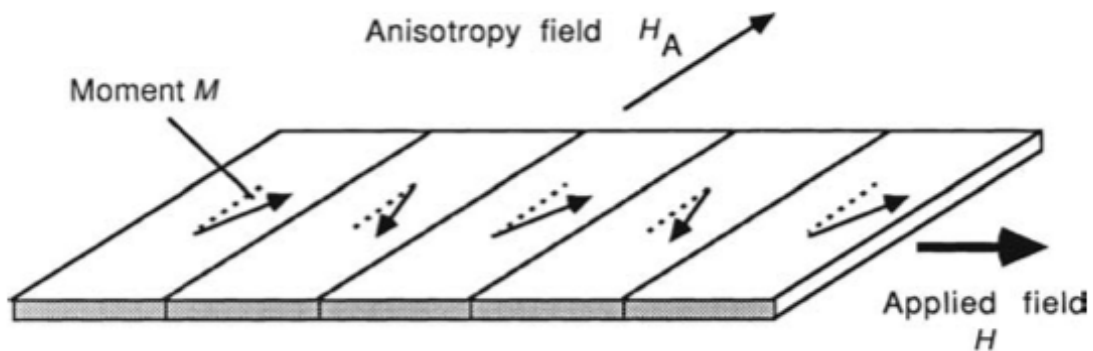


**Figure 2.2** The domain structure in an annealed sample showing the coherent rotation model [20]

According to Ref. [20], the coefficient,  $C$ , is given by

$$C = \frac{3\lambda_s}{2H_A^2} \quad (2.3)$$

Thus, to obtain a large strain, magnetostrictive materials should have a large  $\lambda_s$  and small  $H_A$ . Optimal  $C$  values for a material are often reached after the material has undergone field annealing. Field annealing will be discussed in the following section.

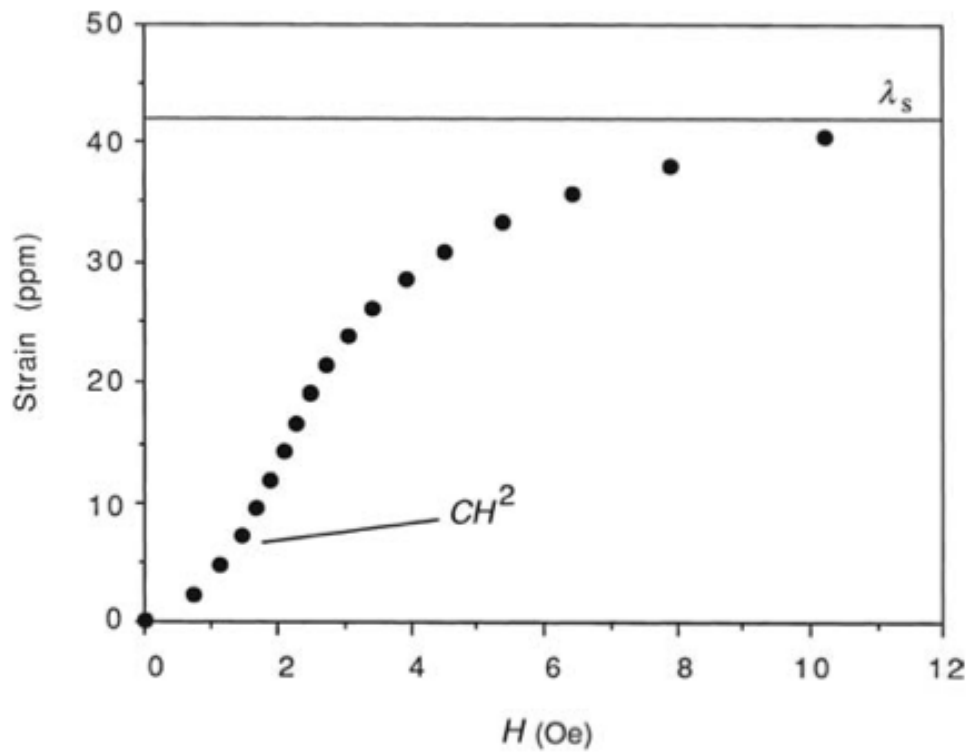


**Figure 2.3** The magnetostrictive response of a material in which the strain approaches the saturation magnetostriction  $\lambda_s$  [20]

### 2.3 Optimizing the Magnetic Field Detection Sensitivity

To optimize the sensitivity of the magnetostrictive sensor, two main methods have been used: field annealing and efficient coupling. The first method, field annealing, involves a heat treatment process of the magnetostrictive material in the presence of a static magnetic field. For the magnetostrictive material Metglas, this process involves heating the material under either vacuum or dry argon gas to its Curie temperature in the presence of a 0.01 – 0.1 T magnetic field, and then slowly cooling it in the presence of the field [20]. A material's Curie temperature is the critical temperature for a ferromagnetic material, defined as the temperature below which spontaneous magnetization occurs in the absence of an externally applied magnetic field [22]. A graph comparing the magnetostriction strain at low magnetic fields before and after annealing is shown in Figure 2.4. The saturation magnetostriction,  $\lambda_s$ , remains relatively unchanged by the field annealing process [22].

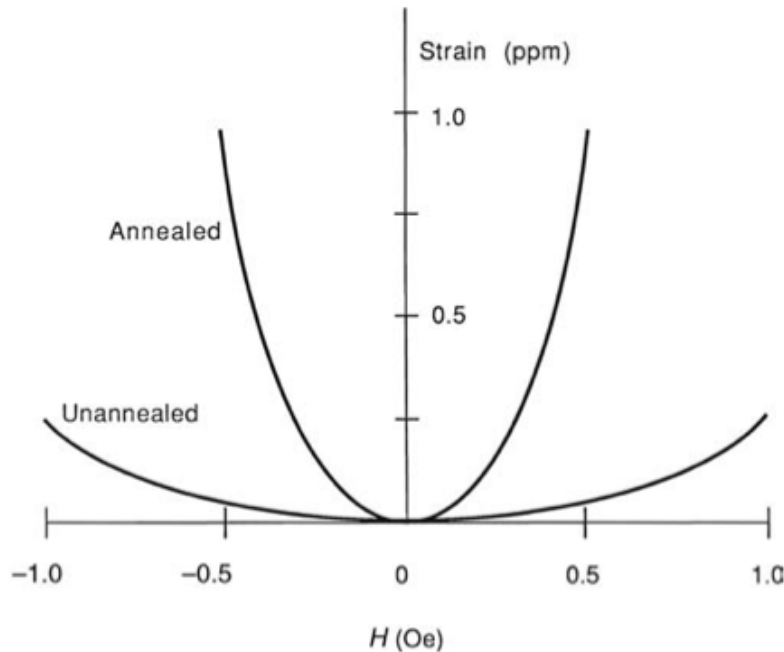


**Figure 2.4** Comparison of the magnetostriction at low magnetic fields before and after field annealing [20].  
1 Oe = 79.77 A/m

A second method of maximizing the detection sensitivity of the magnetostrictive sensor is the efficient coupling of the magnetostrictive material and the optical fiber. According to Ref. [21], there are several methods used to couple the magnetostrictive material to the optical fiber, including evaporation, sputtering, electroplating, and epoxy adhesion. Evaporation, sputtering, and electroplating involve coating the fiber by depositing the magnetostrictive material directly onto the optical fiber. In the epoxy adhesion technique, a ribbon, slab, or cylinder of the magnetostrictive material is coupled to the fiber. These methods allow the magnetostrictive material to be more efficiently coupled to the fiber and, along with field annealing, provide a greater detection of the magnetic field.

## 2.4 Magnetostrictive Materials

Three magnetostrictive materials commonly used in experiments are Terfenol-D, Metglas #2605SC, and nickel. Properties of these three materials are listed in Table 2.1. The magnetic anisotropy field of nickel and Terfenol-D are not readily available, and thus values for this term are not included in Table 2.1. Each of these materials has been used with optical fibers and each offers certain advantages. Other magnetostrictive materials that have been used for similar magnetic sensor applications include TbFeCo alloys,  $\text{SmFe}_2$ ,  $\text{CoFe}_2\text{O}_4$ ,  $\text{Fe}_{85}\text{Ga}_{15}$ ,  $\text{Fe}_{80}\text{Ga}_{20}$ , Fe-Al alloys,  $\text{Ni}_{98}\text{Ga}_2$ , and  $\text{Ni}_{98}\text{Ga}_7$  [29]. Further research is needed to determine the feasibility of using these alternative materials for MEG applications. Both nickel and Terfenol-D are polycrystalline materials, whereas Metglas is an amorphous compound containing silicon and other components. As stated in Ref. [21], nickel is used because it contains randomly aligned magnetic domains,

| Material                     | Melting Temperature [°C] | Saturation Magnetostriction ( $\lambda_s$ ) [ppm] | Curie Temperature [°C] | Magnetic Anisotropy Field ( $H_A$ ) [A/m] |
|------------------------------|--------------------------|---|------------------------|---|
| Nickel [21, 23]              | 1455                     | -33   | >500                   | ?   |
| Metglas #2605SC [24, 25, 26] | ?                        | 27  | 399                    | 70  |
| Terfenol-D [21, 27]          | 1240                     | 1620  | 380                    | ?   |

which helps to facilitate magnetization after field annealing. Terfenol-D has the lowest magnetocrystalline anisotropy of these three compounds. This low magnetocrystalline anisotropy results in a larger magnetostrictive constant,  $C$ , and a larger magnetostriction,  $\epsilon$ , according to equations 2.2 and 2.3. Terfenol-D is comprised of  $TbFe_2$  and  $DyFe_2$ , which both produce large magnetostrictive strain at very high magnetic field strengths. By combining these two compounds in a stoichiometric ratio of  $Tb_{0.3}Dy_{0.7}Fe_2$ , researchers were able to retain the large magnetostrictive properties in Terfenol-D at relatively low annealing field strengths. However, Terfenol-D has not been shown to produce strain in low magnetic fields and low frequency regions [19]. Because the Naval Ordnance Laboratory developed Terfenol-D, commercial availability of this material is also limited. The third material, Metglas, is useful for magnetostrictive sensors because of its amorphous structure, which has no magnetic domains at the macroscopic level [21]. The alloy typically used in magnetostrictive sensors is Metglas #2605SC because it has the highest saturation magnetostriction,  $\lambda_s$ , of the available Metglas alloys. This particular alloy is the compound  $Fe_{81}B_{13.5}Si_{3.5}C_2$  [26]. Metglas is typically available in a thin ribbon form because of its production process, but it is also available through deposition. One portion of the process involves rapidly quenching the molten material to

avoid the formation of crystals in the structure [21]. Due to this part of the process, the thickness of the material is limited. According to Ref. [21], experimental results have concluded that Metglas transducers typically work better in the detection of small magnetic fields, and nickel transducers work better in the detection of large magnetic fields. When the output signals of different magnetic sensors were compared, researchers found that Metglas alloy transducers' output response became saturated near a lower magnetic field of 79.6 A/m<sup>2</sup>, whereas the output response of the nickel transducer remained linear up to a higher magnetic field of 796 A/m<sup>2</sup> [30]. So, these three materials can each be used for magnetostrictive sensors, but each has advantages depending on the application.

## 2.5 Faraday Effect Sensors

A second type of fiber-optic-based magnetic sensor is a Faraday effect sensor. The Faraday effect, discovered in 1845 by Michael Faraday, involves an interaction between light and a magnetic field within a medium [31]. When light is transmitted through a magnetic field in a medium, a change occurs in the polarization of the light, which is proportional to the strength of the magnetic field. The Faraday effect is described by the equation

$$\theta = VLH, \quad (2.4)$$

where  $\theta$  is the angle of rotation,  $V$  is the Verdet constant,  $L$  is the length of the path, and  $H$  is the magnetic field strength. The Verdet constant is a property of the optical material used and describes the strength of the Faraday effect in that material. This phenomenon is shown in Figure 2.5. As light passes through the magnetic field, its polarization rotates

by an angle  $\theta$  due to the Faraday effect [20]. As this angle changes, the state of polarization of the light also changes. The state of polarization refers to the behavior of the electric field vector of a light wave as a function of time. If the state of polarization changes as light moves through a material, the material is birefringent. A birefringent material will have two different indices of refraction. These different refractive indices will cause the orthogonal components of an electric field to become out of phase as the electric field propagates through the material. As one component of the electric field changes, the polarization state changes. This is shown in Figure 2.6. The total change in the state of polarization is dependent on the path of the light in the material, the strength of the birefringence, and the state of polarization.

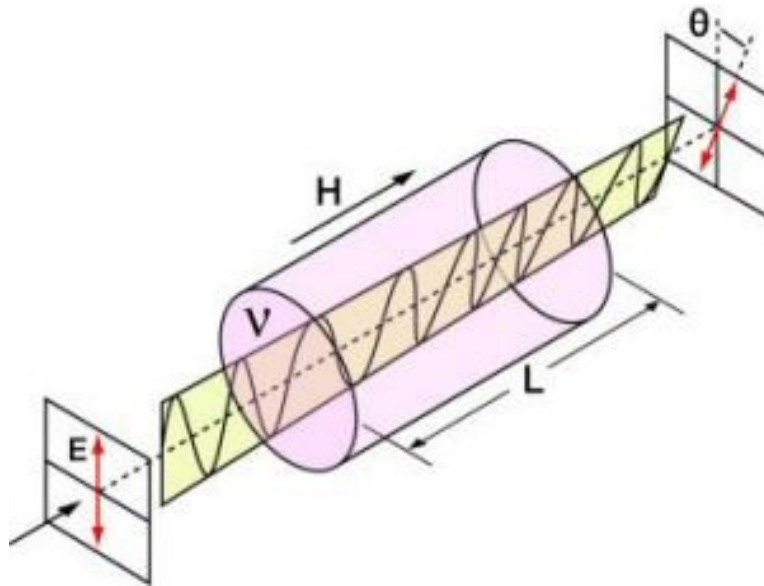


**Figure 2.5** The Faraday effect in a material [32]

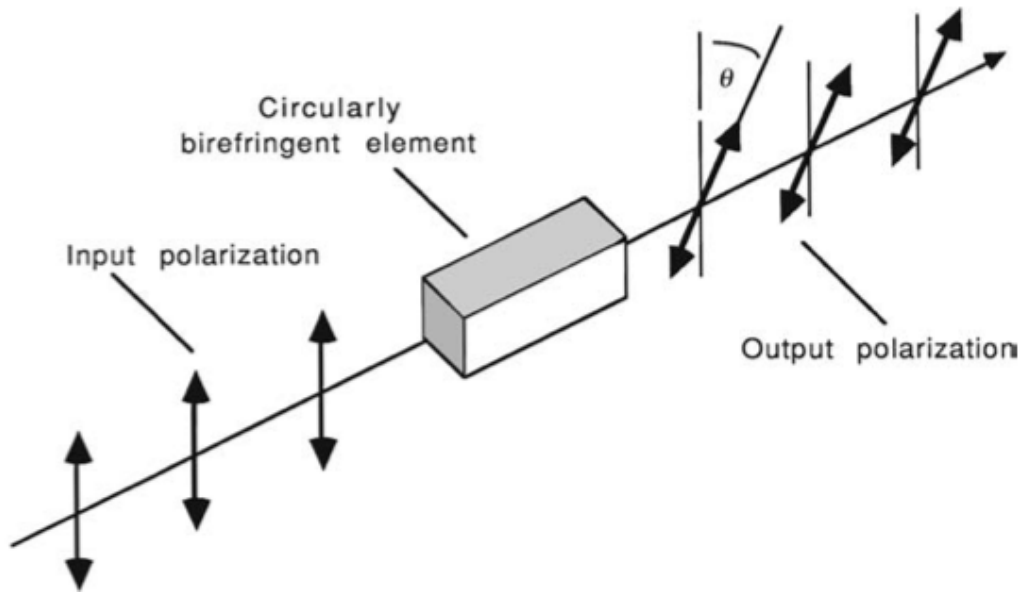


**Figure 2.6** Rotation of the plane of polarization of a linearly polarized light by a circularly birefringent element [20]

The Faraday effect can be used to determine the change in state of light polarization within an optical fiber caused by an applied magnetic field. Faraday found that certain materials induce a circular birefringence in response to an external magnetic field. Fiber optic magnetic sensors based on the Faraday effect, known as Faraday effect sensors, utilize this phenomenon. In these sensors, an externally applied magnetic field causes the plane of polarization of the linearly polarized light propagating in the optical fiber to rotate [21]. Polarizers on the input and analyzers on the output detect this rotation. The Faraday effect involves direct interaction between the externally applied magnetic field and the light propagating through the optical fiber. Thus, Faraday effect sensors are a second type of fiber-optic-based magnetic sensor and involve a linear process. In order to remove the Faraday effect when using a magnetostrictive fiber-optic-based magnetic sensor, a polarization maintaining (PM) fiber can be used.

## 2.6 Lorentz Force Sensors

A third type of fiber-optic-based magnetic sensor is a Lorentz force sensor. Similar to magnetostriction sensors, these sensors involve a dimensional change in an optical fiber due to the presence of a magnetic field [20]. A charge moving in a magnetic field experiences a force, known as the Lorentz force. This force is given by

$$\mathbf{F} = i\mathbf{L} \times \mathbf{B}, \quad (2.5)$$

where  $i$  is the current,  $L$  is the length of the fiber, and  $\mathbf{B}$  is the magnetic flux density. The effects of the Lorentz force can be applied to an optical fiber sensor. The transducer model in Figure 2.7 shows such an example, in which an aluminum-jacketed optical fiber is supported on either end by two clamps. A current,  $i$ , moves through the conductive coating of the fiber in the presence of an applied magnetic field perpendicular to current. The resulting Lorentz force is perpendicular to both the current and the magnetic field and acts uniformly across the entire length of the fiber. Thus, the strain behavior of the optical fiber resulting from the Lorentz force sensor is similar to that of the magnetostrictive sensor. As opposed to the Faraday effect sensors in which the interaction with the external magnetic field takes place directly within the optical fiber itself, in magnetostrictive sensors and Lorentz force sensors, the optical fiber measures the response of a material to the externally applied magnetic field. In order to remove the Lorentz force when using a magnetostrictive fiber-optic-based magnetic sensor, the magnetostrictive film can be open-circuited to prevent current flow.

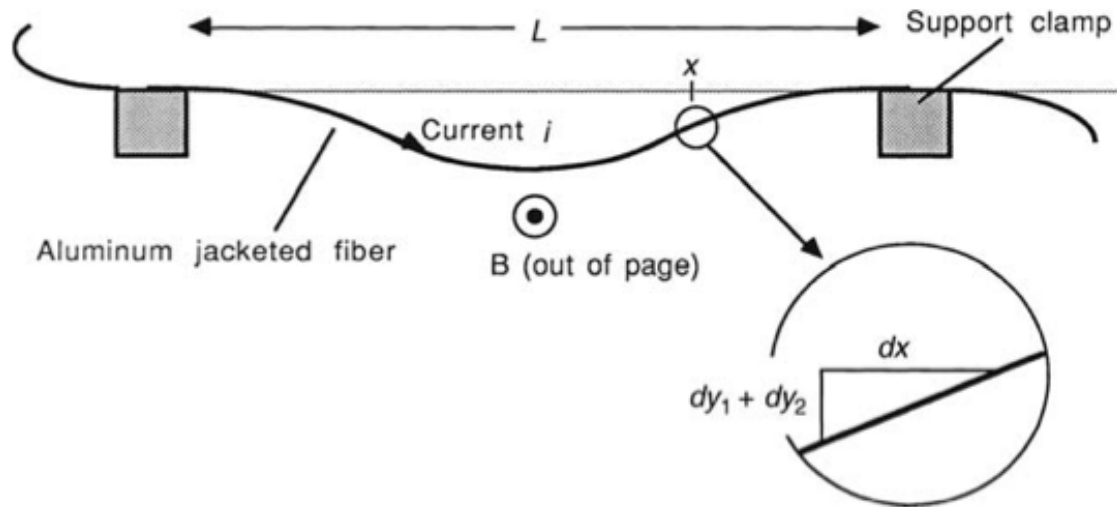


**Figure 2.7** A transducer model for a Lorentz force sensor [20]

## 2.7 Advantages of Fiber Optic Sensors Over SQUID

In MEG, SQUIDs are currently used to detect magnetic fields. SQUID sensors can measure between  $10^{-14}$  and  $10^{-7}$  T [33]. However, the large size and high cost of current MEG systems, due to the SQUID sensors, pose a disadvantage. Fiber-optic-based magnetic sensors are small and inexpensive [34]. The lengths of the magnetostrictive materials are generally on the order of centimeters. They are also able to operate at room temperature and are relatively simple to both operate and manufacture. According to Ref. [21], fiber optic sensors can currently detect as low as  $1.3 \times 10^{-11}$  T. Thus, fiber-optic-based magnetic sensors may present a useful and practical alternative to SQUID sensors.

## 2.8 Conclusion

Fiber-optic-based magnetic sensors are one of the many methods used for magnetic field sensing. These sensors offer many advantages over other techniques, such as a small size, low weight, and low cost. With these benefits, fiber optic sensors have the potential to enhance current applications of magnetic field sensing, such as MEG.

## SECTION 3: EXPERIMENTAL SETUP

### 3.1 Introduction

Magnetostrictive fiber-optic-based magnetic sensors are one way to sense a magnetic field, as explained in the previous section. Because of their added benefits over other magnetic sensors, they may allow for a useful alternative to the SQUID sensors currently being used in MEG systems. To determine and evaluate their potential use and effectiveness compared to the current technology, we describe an experiment to characterize the sensitivity of magnetostrictive fiber-optic-based magnetic sensors using a Mach-Zehnder interferometer.

### 3.2 Mach-Zehnder Interferometer

Magnetostrictive fiber-optic-based magnetic sensors use interferometers to measure the magnetostriction in a transducing material. One type of interferometer, the Mach-Zehnder interferometer, is shown in Figure 2.1, which is included again as Figure 3.1. A typical Mach-Zehnder interferometer consists of two couplers, one at the input and one at the output [35]. It also consists of two arms, the reference arm and the sensing arm. In Figure 3.1, the reference arm is upper arm and the sensing arm is the lower arm with the magnetostrictive sensing element. Light from a laser is passed through a fiber. The light is then split into two beams by a coupler with part of the light moving through the reference arm and part moving through the sensing arm. The second coupler recombines these two outputs. A photodetector then detects the interference pattern between the two beams of light, after they have propagated the length of the output fiber.

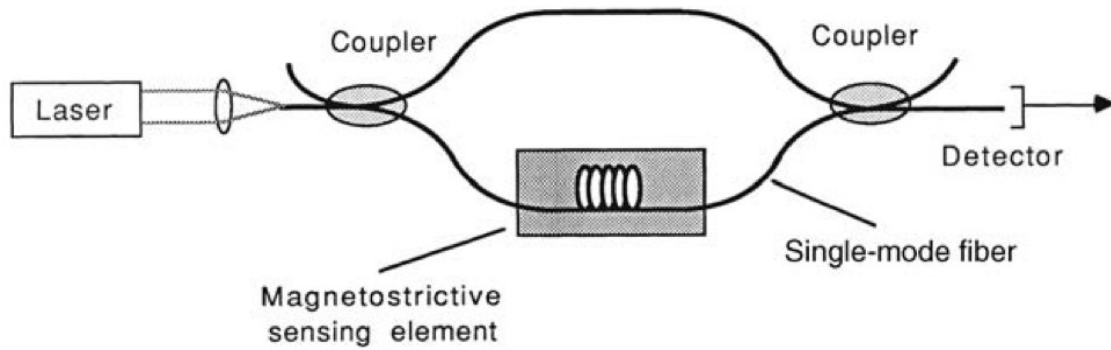


**Figure 3.1** Mach-Zehnder interferometer schematic with a magnetostrictive fiber optic magnetometer [20]

The reference arm is often wrapped around a phase shifter to be used in a demodulation approach.

### 3.3 Experimental Setup

In the setup for this project, a polarization maintaining fiber will be used to eliminate the Faraday effect, as previously noted in section 2.4. The optical fiber in the reference arm will be wrapped around a piezoelectric tube, as shown in Figure 3.2. This tube is ceramic and has metal coating on its inner and outer surface. This tube is often a lead zirconate titanate tube, or PZT tube, which has a high piezoelectric coefficient. When a voltage is applied across the PZT tube, it will expand [36]. This phenomenon is known as the converse piezoelectric effect. By wrapping the fiber around the PZT tube, the stretching of the fiber can be controlled.

When a magnetic field is applied to the sensing arm, the magnetostrictive coating will expand, stretching the fiber. As this fiber is stretched, there becomes a phase difference between the light in the sensing arm and the light in the reference arm. The phase difference is known as the optical path difference, or OPD. As this OPD changes,

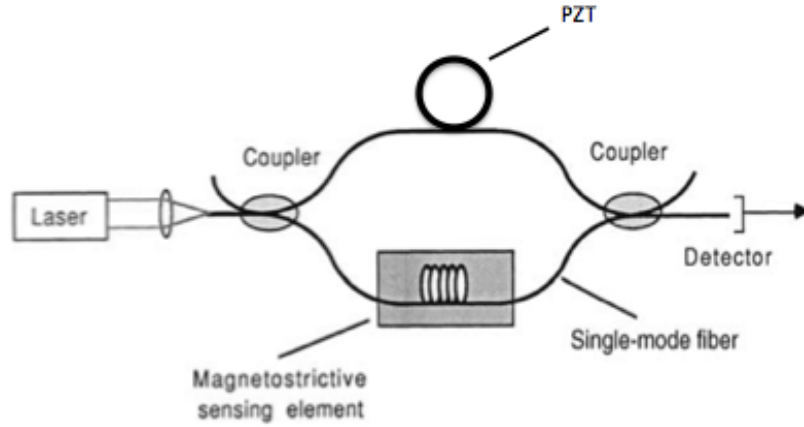


**Figure 3.2** A Mach-Zehnder interferometer schematic with a magnetostrictive fiber optic magnetometer and PZT tube [20]

the irradiance of light detected by the photodetector will change. In order to make more precise changes to this intensity, the reference arm is stretched using the PZT tube. By stretching the reference arm fiber in a well-controlled manner, the magnitude of the magnetic field applied to the reference arm can be determined.

### 3.4 Interferometer Signal

The instantaneous electric field of the light on the detector contributed by the reference arm is given by

$$E_r = E_{r0} \cos(\omega_0 t - kx_r), \quad (3.1)$$

where  $E_{r0}$  is the reference field amplitude,  $\omega_0$  is the optical angular frequency,  $k$  is the propagation constant in air, and  $x_r$  is the amount the reference path is stretched. In this equation,

$$x_r = A_r \sin(\omega_r t), \quad (3.2)$$

where  $A_r$  is the amplitude and  $\omega_r$  is the angular frequency. The propagation constant,  $k$ , is given by

$$k = \frac{2\pi n}{\lambda}, \quad (3.3)$$

where  $n$  is the optical fiber mode index and  $\lambda$  is the optical wavelength. Similarly, the instantaneous electric field contributed by the signal arm is described by

$$E_s = E_{s0} \cos(\omega_0 t - kx_s), \quad (3.4)$$

where  $E_{s0}$  is the reference field amplitude,  $\omega_0$  is the optical angular frequency,  $k$  is the propagation constant in air, and  $x_s$  is the amount the signal path is being stretched. Here,  $k$  is also given by equation 3.3. In this equation,

$$x_s = L\epsilon(H)\xi\eta, \quad (3.5)$$

where  $\epsilon$  is the strain of the material,  $H$  is the externally applied magnetic field,  $L$  is the interaction length of the fiber,  $\eta$  is the strain transfer efficiency, and  $\xi$  is the strain optic correction factor that accounts for the strain coupling efficiency between the magnetostrictive film and the optical fiber. Using equation 2.3 and separating the magnetic field into its dc and ac components, this becomes

$$x_s = L\xi\eta \left( \frac{3\lambda_s}{2H_A^2} \right) [H_0 + H_\Omega \sin\Omega t]^2, \quad (3.6)$$

where  $\lambda_s$  is the saturation magnetostriction,  $H_A$  is the anisotropy field,  $H_0$  is the dc magnetic field,  $H_\Omega$  is the zero-to-peak amplitude of the magnetic field, and  $\Omega$  is the angular frequency of the magnetic field.

The superposition of these two electric fields results in interference patterns whose power is related to the optical path difference, OPD, between the two arms of the interferometer. To determine an expression for the output optical power,  $P_o$ , it is noted

that the output power is proportional to the squared magnitude of the superposition of the reference and signal electrical fields, as shown by

$$P_o \propto |E_r + E_s|^2. \quad (3.7)$$

Substitution and manipulation of the real parts of equations 3.1 and 3.4 into 3.7 yields

$$P_o \propto 2E_0^2 \{1 + \cos \phi\}, \quad (3.8)$$

where

$$\phi = -k(x_r + x_s) - \cos \phi \quad (3.9)$$

and  $E_0 = E_{r0} = E_{s0}$ . Due to the averaging effects of the photodetector, it will not be able to detect the optical frequencies of the  $\omega_0$  term in equations 3.1 and 3.4. So, those frequency terms were dropped in equation 3.8.

Based on equation 3.8, the photodetector current,  $I_p$ , is given by

$$I_p \propto P_o \propto 1 + M \cos[k(x_r - x_s) - \phi], \quad (3.10)$$

where  $M$  is the fringe contrast due to the unequal signal and reference amplitudes, polarization states of the signal and reference beams, and the coherence between the signal and reference beams. This fringe contrast,  $M$ , is given by values  $0 \leq M \leq 1$ . In equation 3.10,  $\phi$  accounts for practical effects, such as drift of the interferometer. Equation 3.10 plotted in the time domain and frequency domain is shown in Figures 3.3 and 3.4, respectively. The subsequent analysis describes a demodulation algorithm for the previously described experimental system. This demodulation algorithm extracts information from the change in light measured to determine the corresponding magnetic field. In this algorithm, the signals of three frequencies,  $\Omega$ ,  $\omega_r$ , and  $\omega_r - \Omega$ , are evaluated.

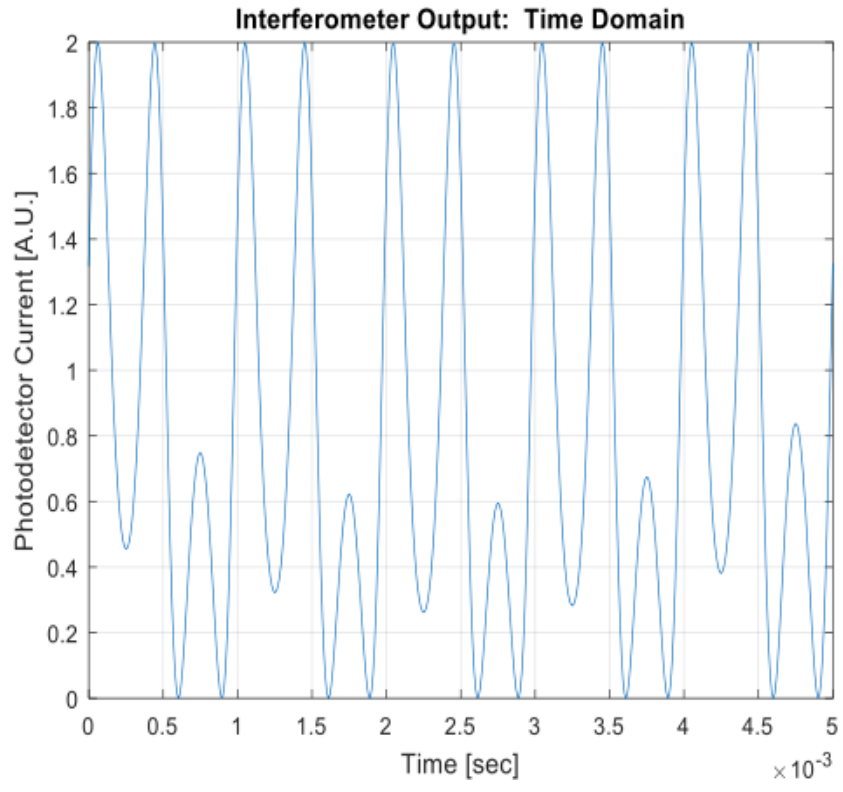


**Figure 3.3** The time domain of the interferometer signal

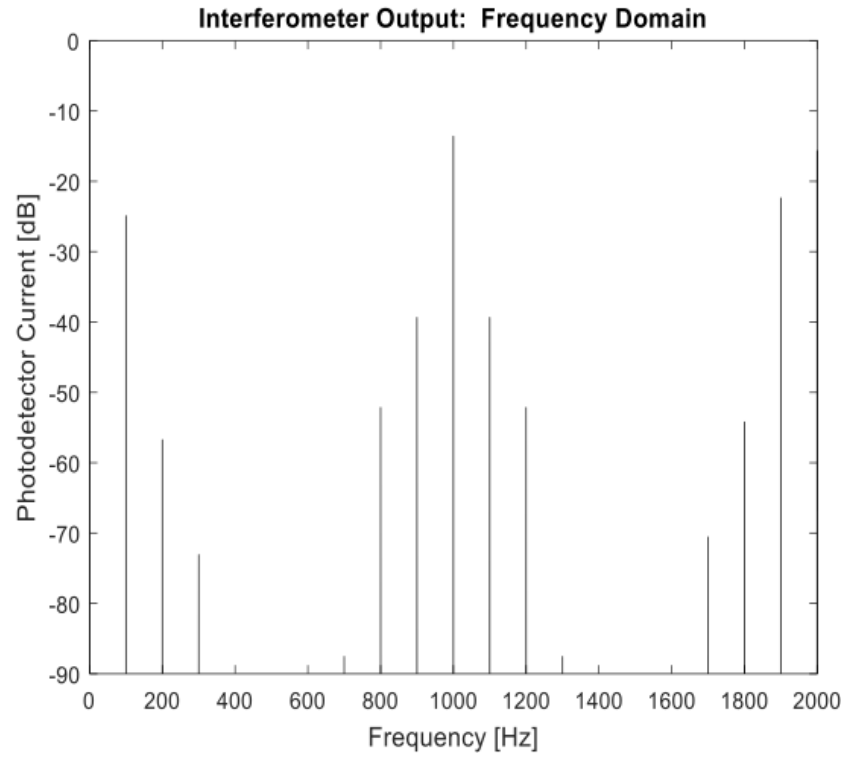


**Figure 3.4** The frequency domain of the interferometer signal

Substituting equations 3.2 and 3.6 into equation 3.9 results in the relationship

$$\phi = k \left( A_r \sin(\omega_r t) + L\xi\eta \left( \frac{3\lambda_s}{2H_A^2} \right) (H_o^2 + 2H_o H_\Omega \sin \Omega t + H_\Omega^2 (\sin \Omega t)^2) \right) - \phi. \quad (3.11)$$

Substitution of relation (3.3) into (3.10) and subsequent rearrangement of relation (3.10)

using the trigonometric identity for the  $(\sin \Omega t)^2$  term yields,

$$\begin{aligned} \phi = & \frac{2\pi n}{\lambda} L\xi\eta \left( \frac{3\lambda_s}{2H_A^2} \right) \left( H_o^2 + \frac{H_\Omega^2}{2} \right) + \frac{4\pi n}{\lambda} L\xi\eta \left( \frac{3\lambda_s}{2H_A^2} \right) H_o H_\Omega \sin \Omega t \\ & - \frac{\pi n}{\lambda} L\xi\eta \left( \frac{3\lambda_s}{2H_A^2} \right) H_\Omega^2 \cos(2\Omega t) + \frac{2\pi n}{\lambda} A_r \sin \omega_r t - \phi, \end{aligned} \quad (3.12)$$

where the first term is the dc component, the second term is the frequency component which varies as  $\Omega$ , the third term is the frequency component which varies as  $2\Omega$ , and the fourth term is the high frequency component which varies as  $\omega_r$ . Redefining these terms yields

$$A = \frac{2\pi n}{\lambda} L\xi\eta \left( \frac{3\lambda_s}{2H_A^2} \right) \left( H_o^2 + \frac{H_\Omega^2}{2} \right) \quad (3.13)$$

$$B = 2 \frac{2\pi n}{\lambda} L\xi\eta \left( \frac{3\lambda_s}{2H_A^2} \right) H_o H_\Omega \sin \Omega t \quad (3.14)$$

$$C = -\frac{R}{2} H_\Omega^2 \sin \left( 2\Omega t + \frac{\pi}{2} \right) \quad (3.15)$$

$$D = -k A_r \sin \omega_r t, \quad (3.16)$$

$$E = -\phi \quad (3.17)$$

Substituting these terms into (3.10) yields

$$I_p \propto P_o \propto 1 + M \cos(A + B + C + D + E). \quad (3.10)$$

Using the sum and difference trigonometric identities, relation (3.18) becomes

$$\begin{aligned} I \propto \text{Re}\{E_{r0} E_{s0}^*\} & [\cos A \cos B \cos C \cos D \cos E \\ & - \sin A \sin B \cos C \cos D \cos E \end{aligned}$$

$$\begin{aligned}
& - \sin A \cos B \sin C \cos D \cos E \\
& - \cos A \sin B \sin C \cos D \cos E \\
& - \sin A \cos B \cos C \sin D \cos E \\
& - \cos A \sin B \cos C \sin D \cos E \\
& - \cos A \cos B \sin C \sin D \cos E \\
& + \sin A \sin B \sin C \sin D \cos E \\
& - \sin A \cos B \cos C \cos D \sin E \\
& - \cos A \sin B \cos C \cos D \sin E \\
& - \cos A \cos B \sin C \cos D \sin E \\
& + \sin A \sin B \cos C \sin D \sin E \\
& + \sin A \cos B \sin C \sin D \sin E \\
& + \cos A \sin B \sin C \sin D \sin E. \tag{3.19}
\end{aligned}$$

This expression for the signal current, however, does not show the harmonic context of the output signal of the interferometer. Utilizing the component parts of the Jacobi-Anger expansion shows this harmonic content of the output signal [36]. These component parts are shown by

$$\cos[z \cos \theta] = J_0(z) + 2 \sum_{n=1}^{\infty} (-1)^n J_{2n}(z) \cos(2n\theta), \tag{3.20}$$

$$\sin[z \cos \theta] = -2 \sum_{n=1}^{\infty} (-1)^n J_{2n-1}(z) \cos[(2n-1)\theta], \tag{3.21}$$

$$\cos[z \sin \theta] = J_0(z) + 2 \sum_{n=1}^{\infty} J_{2n}(z) \cos(2n\theta), \tag{3.22}$$

and

$$\sin[z \sin \theta] = 2 \sum_{m=1}^{\infty} J_{2m-1}(z) \sin[(2m-1)\theta], \tag{3.23}$$

where  $J_n$  is the Bessel function of the first kind and order  $n$ . Substitution of equations 3.20 and 3.21 into 3.19 and expansion of the summation yields the following equation containing only the  $\Omega$  frequency terms.

$$\begin{aligned}
& I_p \propto P_o \propto 1 + \\
& M\left[[-2 \sin\left[\left(\frac{2\pi n}{\lambda} L\xi\eta\right)\left(\frac{3\lambda_s}{2H_A^2}\right)\left(H_0^2 + \frac{H_\Omega^2}{2}\right)\right] J_1\left(2\left(\frac{2\pi n}{\lambda} L\xi\eta\right) H_0 H_\Omega\right) J_0\left(-\frac{\left(\frac{2\pi n}{\lambda} L\xi\eta\right)}{2} H_\Omega^2\right) J_0(-kA_r) \cos(\phi)\right. \\
& -2 \sin\left[\left(\frac{2\pi n}{\lambda} L\xi\eta\right)\left(\frac{3\lambda_s}{2H_A^2}\right)\left(H_0^2 + \frac{H_\Omega^2}{2}\right)\right] J_1\left(2\left(\frac{2\pi n}{\lambda} L\xi\eta\right) H_0 H_\Omega\right) J_2\left(-\frac{\left(\frac{2\pi n}{\lambda} L\xi\eta\right)}{2} H_\Omega^2\right) J_0(-kA_r) \cos(\phi) \\
& -2 \sin\left[\left(\frac{2\pi n}{\lambda} L\xi\eta\right)\left(\frac{3\lambda_s}{2H_A^2}\right)\left(H_0^2 + \frac{H_\Omega^2}{2}\right)\right] J_3\left(2\left(\frac{2\pi n}{\lambda} L\xi\eta\right) H_0 H_\Omega\right) J_2\left(-\frac{\left(\frac{2\pi n}{\lambda} L\xi\eta\right)}{2} H_\Omega^2\right) J_0(-kA_r) \cos(\phi) \\
& +2 \sin\left[\left(\frac{2\pi n}{\lambda} L\xi\eta\right)\left(\frac{3\lambda_s}{2H_A^2}\right)\left(H_0^2 + \frac{H_\Omega^2}{2}\right)\right] J_3\left(2\left(\frac{2\pi n}{\lambda} L\xi\eta\right) H_0 H_\Omega\right) J_4\left(-\frac{\left(\frac{2\pi n}{\lambda} L\xi\eta\right)}{2} H_\Omega^2\right) J_0(-kA_r) \cos(\phi) \\
& +2 \cos\left[\left(\frac{2\pi n}{\lambda} L\xi\eta\right)\left(\frac{3\lambda_s}{2H_A^2}\right)\left(H_0^2 + \frac{H_\Omega^2}{2}\right)\right] J_1\left(2\left(\frac{2\pi n}{\lambda} L\xi\eta\right) H_0 H_\Omega\right) J_1\left(-\frac{\left(\frac{2\pi n}{\lambda} L\xi\eta\right)}{2} H_\Omega^2\right) J_2(-kA_r) \cos(\phi) \\
& \left.-2 \cos\left[\left(\frac{2\pi n}{\lambda} L\xi\eta\right)\left(\frac{3\lambda_s}{2H_A^2}\right)\left(H_0^2 + \frac{H_\Omega^2}{2}\right)\right] J_3\left(2\left(\frac{2\pi n}{\lambda} L\xi\eta\right) H_0 H_\Omega\right) J_1\left(-\frac{\left(\frac{2\pi n}{\lambda} L\xi\eta\right)}{2} H_\Omega^2\right) J_0(-kA_r) \cos(\phi)\right] \\
& \cdot \sin(\Omega t)] \tag{3.24}
\end{aligned}$$

Substitution of equations 3.20 and 3.21 into 3.19 and expansion of the summation yields the following equation containing only the  $\omega_r$  frequency terms.

$$\begin{aligned}
& I_p \propto P_o \propto 1 + \\
& M\left[[-2 \sin\left[\left(\frac{2\pi n}{\lambda} L\xi\eta\right)\left(\frac{3\lambda_s}{2H_A^2}\right)\left(H_0^2 + \frac{H_\Omega^2}{2}\right)\right] J_0\left(-\frac{\left(\frac{2\pi n}{\lambda} L\xi\eta\right)}{2} H_\Omega^2\right) J_1(-kA_r) \cos(\phi)\right] \cdot \sin(\omega_r t) \tag{3.25}
\end{aligned}$$

Substitution of equations 3.20 and 3.21 into 3.19 and expansion of the summation yields the following equation containing only the  $\omega_r - \Omega$  frequency terms.

$$I_p \propto P_o \propto 1 +$$

$$\begin{aligned}
& M \left[ -\cos \left[ \left( \frac{2\pi n}{\lambda} L\xi\eta \right) \left( \frac{3\lambda_s}{2H_A^2} \right) \left( H_0^2 + \frac{H_\Omega^2}{2} \right) \right] J_1 \left( 2 \left( \frac{2\pi n}{\lambda} L\xi\eta \right) H_0 H_\Omega \right) J_0 \left( -\frac{\left( \frac{2\pi n}{\lambda} L\xi\eta \right)}{2} H_\Omega^2 \right) J_1(-kA_r) \cos(\phi) \right. \\
& - 2 \cos \left[ \left( \frac{2\pi n}{\lambda} L\xi\eta \right) \left( \frac{3\lambda_s}{2H_A^2} \right) \left( H_0^2 + \frac{H_\Omega^2}{2} \right) \right] J_1 \left( 2 \left( \frac{2\pi n}{\lambda} L\xi\eta \right) H_0 H_\Omega \right) J_2 \left( -\frac{\left( \frac{2\pi n}{\lambda} L\xi\eta \right)}{2} H_\Omega^2 \right) J_1(-kA_r) \cos(\phi) \\
& + 2 \cos \left[ \left( \frac{2\pi n}{\lambda} L\xi\eta \right) \left( \frac{3\lambda_s}{2H_A^2} \right) \left( H_0^2 + \frac{H_\Omega^2}{2} \right) \right] J_3 \left( 2 \left( \frac{2\pi n}{\lambda} L\xi\eta \right) H_0 H_\Omega \right) J_2 \left( -\frac{\left( \frac{2\pi n}{\lambda} L\xi\eta \right)}{2} H_\Omega^2 \right) J_1(-kA_r) \cos(\phi) \\
& + 2 \cos \left[ \left( \frac{2\pi n}{\lambda} L\xi\eta \right) \left( \frac{3\lambda_s}{2H_A^2} \right) \left( H_0^2 + \frac{H_\Omega^2}{2} \right) \right] J_3 \left( 2 \left( \frac{2\pi n}{\lambda} L\xi\eta \right) H_0 H_\Omega \right) J_4 \left( -\frac{\left( \frac{2\pi n}{\lambda} L\xi\eta \right)}{2} H_\Omega^2 \right) J_1(-kA_r) \cos(\phi) \right] \\
& \quad \cdot \cos(\omega_r t - \Omega t) \\
& - \cos \left[ \left( \frac{2\pi n}{\lambda} L\xi\eta \right) \left( \frac{3\lambda_s}{2H_A^2} \right) \left( H_0^2 + \frac{H_\Omega^2}{2} \right) \right] J_1 \left( 2 \left( \frac{2\pi n}{\lambda} L\xi\eta \right) H_0 H_\Omega \right) J_0 \left( -\frac{\left( \frac{2\pi n}{\lambda} L\xi\eta \right)}{2} H_\Omega^2 \right) J_1(-kA_r) \sin(\phi) \\
& \quad \cdot \sin(\omega_r t - \Omega t) \tag{3.26}
\end{aligned}$$

As noted, the terms in equations 3.24-3.26 show only the  $\Omega$ ,  $\omega_r$ , and  $\omega_r - \Omega$  frequencies, although the complete signal includes many more frequencies.

Using simulated amplitudes of the three frequency components, given in equations 3.24 – 3.26, the values for  $M$ ,  $H_\Omega$ , and  $\phi$  can be determined. The amplitudes of these three frequency components are shown in Figure 3.5, indicated by the red circles and the corresponding frequency written above the circle.

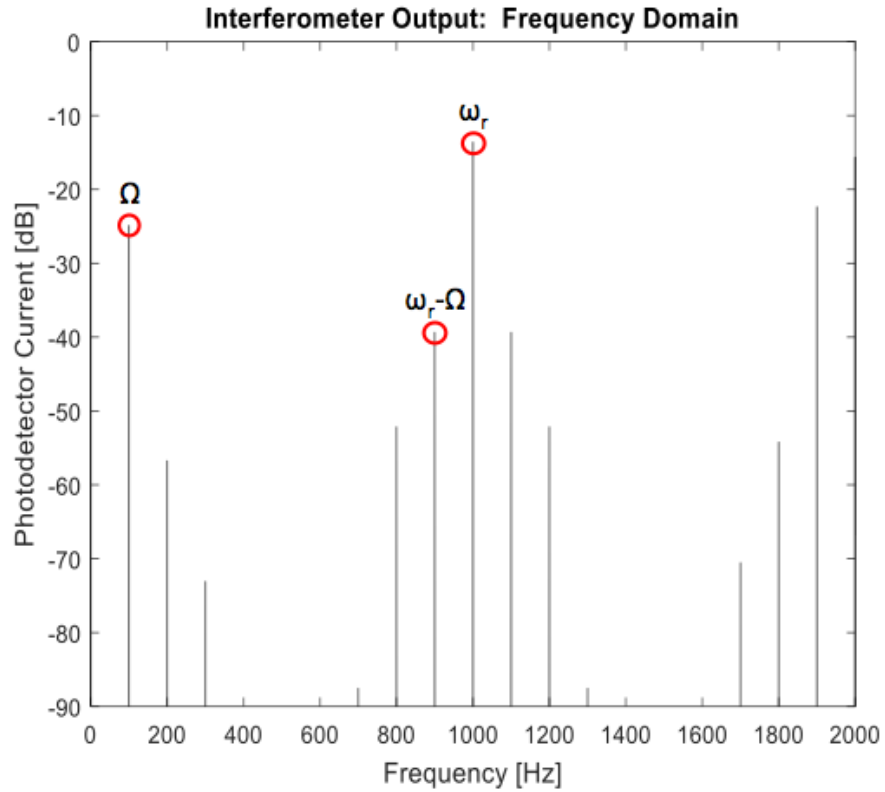


**Figure 3.5** The frequency response of the experimental system, showing the three frequencies of interest

### 3.5 Conclusion

The experimental setup explained in this section will allow for a magnetic field to be sensed by a magnetostrictive fiber-optic-based magnetic sensor. These magnetostrictive fiber-optic-based sensors may provide an effective alternative to the current SQUID sensors, creating a smaller and less expensive MEG system. Further analysis and verification of the derived photodetector signal is needed before the experiment is performed.

## SECTION 4: Ultimate Resolution of an Interferometric Magnetic Sensor

### 4.1 Introduction

The strengths of magnetic fields produced in the brain are very weak and typically range from  $10^{-14}$  to  $10^{-13}$  T, as previously discussed in section 1. The magnetic field sensors currently used in MEG systems, SQUIDs, can measure as low as 10 fT at frequencies from dc to 1 kHz. The range of detectable magnetic field values using a magnetostrictive fiber-optic-based magnetic sensor depends on the magnetostrictive material used. Current magnetostrictive materials, such as Terfenol-D, have the potential to reach the magnetic flux density values produced by the brain.

### 4.2 Theory and Analysis

The minimum detectable magnetic flux density of a magnetic sensor, based on a fundamental physical limitation of the system, is the “ultimate resolution” of the magnetic sensor. For optical interferometric sensors, that fundamental physical limitation determining the smallest magnetic flux density that the optically based system can detect is the quantum nature of light in the photodetection process. In this process, a single photon of light produces a single electron-hole pair in a semiconductor photodetector. This electron-hole pair is generated when an electron absorbs sufficient light energy to move into the conduction band of the semiconductor, leaving a hole in the valence band. The creation of this electron-hole pair allows for the absorption of photons [38]. This characteristic for a specific sensor configuration limits the smallest detectable magnetic

flux density that an optically based sensor can detect, meaning that no enhancement in resolution is possible.

To characterize the magnetostrictive properties of metal-coated optical fibers, a fiber interferometer using the phase-generated carrier, or PGC, demodulation technique is explored. In this configuration, a carrier is imposed on the signal by straining the interferometer's reference arm with a PZT, or lead zirconate titanate, tube, as explained in section 3.3. By wrapping the optical fiber around the PZT tube, the stretching of the fiber can be controlled. Figure 4.1 shows this interferometric configuration.

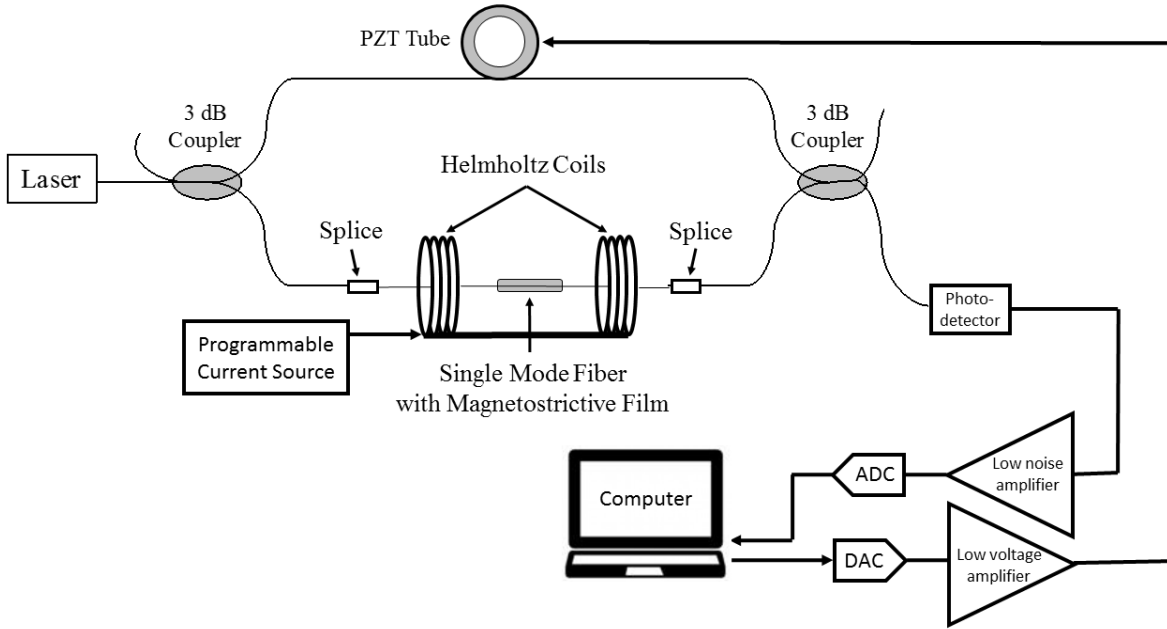


**Figure 4.1** A 2-beam interferometer used to characterize the magnetostrictive properties of metal-coated optical fibers. ADC is an analog-to-digital converter, and DAC is a digital-to-analog converter.

According to [39], for interferometers using this PGC demodulation scheme, the quantum-noise-limited signal-to-noise ratio, SNR, as a function of the detected phase change of the interferometer,  $\Delta\phi$ , is given by

$$\text{SNR} = \left( \frac{P_i \eta_{\text{det}}}{h\nu \Delta\nu} \right)^{1/2} \Delta\phi \times \left[ \frac{1 - J_0(2\pi) \cos(4k_o\Delta)}{2 + 2J_0(\pi) \cos(2k_o\Delta) - 4\Delta\phi J_0(\pi) \sin(2k_o\Delta)} \right]^{1/2}, \quad (4.1)$$

where  $P_i$  is the laser input power,  $\eta_{\text{det}}$  is the photodetector quantum efficiency,  $h$  is Planck's constant,  $\nu$  is the frequency of the light in Hz,  $c$  is the free space speed of light,  $\lambda$  is the free space wavelength of the light,  $\Delta\nu$  is the detection electronics bandwidth, and  $\Delta$  is the path length difference between the interferometer arms. The values used for the analysis of the proposed system and constant values are given below.

$$\begin{aligned}
P_i &= 10 \text{ mW}, \\
\eta_{\text{det}} &= 45\%, \\
h &= 6.62617 \times 10^{-34} \text{ J} \cdot \text{s}, \\
\nu &= c/\lambda, \\
c &= 2.9979 \times 10^8 \text{ m/s}, \\
\lambda &= 850 \text{ nm}, \\
\Delta\nu &= 1 \text{ kHz}, \\
k_o &= \frac{2\pi}{\lambda} (\text{m}^{-1}), \text{ and} \\
\Delta &= 0.25\lambda
\end{aligned}$$

The phase change of the interferometer,  $\Delta\phi$ , is related to the difference in the path length between the signal and reference arms of the interferometer. This phase change is produced by the strain induced by the magnetic field in the optical fiber. As shown in Ref. [20], the magnetic field-dependent phase change is given by

$$\Delta\phi = \left(\frac{2\pi}{\lambda}\right) nL\xi\eta_{\text{film}} \left(\frac{3\lambda_s}{2H_A^2}\right) H^2, \quad (4.2)$$

where  $n$  is the refractive index of the fiber core,  $L$  is the interaction length between the optical fiber and the metal coating,  $\xi$  is the strain optic correction factor between the fiber strain and the optical mode,  $\eta_{\text{film}}$  is the strain transfer efficiency between the metal film and optical fiber,  $\lambda_s$  is the saturation magnetostriction of the metal film, and  $H_A$  is the anisotropy field of the metal film. The typical system parameter values for the proposed system are given below.

$$\begin{aligned}
n &= 1.46, \\
\xi &= 78\%, \\
\eta_{\text{film}} &= 90\%,
\end{aligned}$$

The magnetic-field-induced strain of the magnetostrictive material is given by equations 2.2 and 2.3. Combining these equations gives

$$\epsilon = \left( \frac{3\lambda_s}{2H_A^2} \right) H^2. \quad (4.3)$$

This equation describes the “coherent rotation model” of magnetostriction, which assumes that the material has a uniaxial anisotropy that defines an easy axis that is characterized by an anisotropy field  $H_A$  [20]. When no external magnetic field is applied, the magnetic moments in the material will point in the positive or negative direction along the direction of the anisotropy field, which is the “easy axis.” The strength of this anisotropy field controls how “tightly” the moments are held along the easy axis. Thus, a low anisotropy field results in an easier rotation of the moments, producing the resulting magnetostrictive strain [26]. Once an external magnetic field is applied, the moments rotate coherently away from their easy axis and toward the direction of the applied field.

Magnetostrictive fiber-optic-based magnetic sensors normally operate with a dc bias magnetic field  $H_{dc}$ . This dc magnetic field increases the sensor’s sensitivity to the small amplitude of the ac magnetic field. The applied magnetic field, including the dc component, can be defined as  $H = H_{dc} + \Delta H_{min} \cos \omega t$ , where  $\Delta H_{min}$  is the peak amplitude of the smallest detectable ac magnetic field. Applying a small signal analysis linearizes the strain’s magnetic field dependence at an operating point that is set by the dc bias field  $H_{dc}$ . Using this analysis, the quadratic dependence of  $\Delta\phi$  and  $H$  in equation 4.2 becomes a linear dependence of  $\Delta\phi_{min}$ , the minimum detectable phase change, and  $\Delta H_{min}$ . Equation 4.2 then becomes

$$\Delta\phi_{min} = \left( \frac{2\pi}{\lambda} \right) nL\xi\eta_{film} \left( \frac{3\lambda_s}{2H_A^2} \right) (2H_{dc})\Delta H_{min}. \quad (4.4)$$

The  $\Delta\phi_{\min}$  in equation 4.4 can be applied as the  $\Delta\phi$  of equation 4.1 if an interferometer is used with PGC demodulation to determine  $\Delta H_{\min}$ . Maintaining convention, the ultimate system resolution is defined at SNR equal to unity.

### 4.3 Metglas

The saturation magnetostriction for Metglas 2605SC is  $\lambda_s = 27 \text{ ppm}$  [25], and its anisotropy field is  $H_A = 70 \text{ A/m}$  [26]. The quantum-noise-limited magnetic flux density,  $B_{\min}$ , for Metglas is plotted in Figure 4.2 as a function of the interaction length,  $L$ , of the metal coating on the fiber. For this plot,  $B_{\min} = \mu_o \Delta H_{\min}$ . This plot was generated using the Matlab code shown in Appendix B. A dc bias field of  $H_{\text{dc}} = 35 \text{ A/m}$  was selected to produce a dc strain sufficiently below the saturation magnetostriction. This value was found using the parameters  $(\epsilon = 10 \times 10^{-6}) < (\lambda_s = 27 \times 10^{-6})$ .

As previously stated, MEG applications require detection of magnetic flux densities ranging from 10 to 100 fT at frequencies from dc for 1 kHz. As shown in Figure 4.2, the smallest detectable magnetic flux density of the sensor using Metglas as the magnetostrictive material is on the order of picotesla, which is considerably larger than the required range for MEG of 10 to 100 fT. Thus, a magnetic field sensor using Metglas will not have sufficient resolution for the application of detecting brain waves.

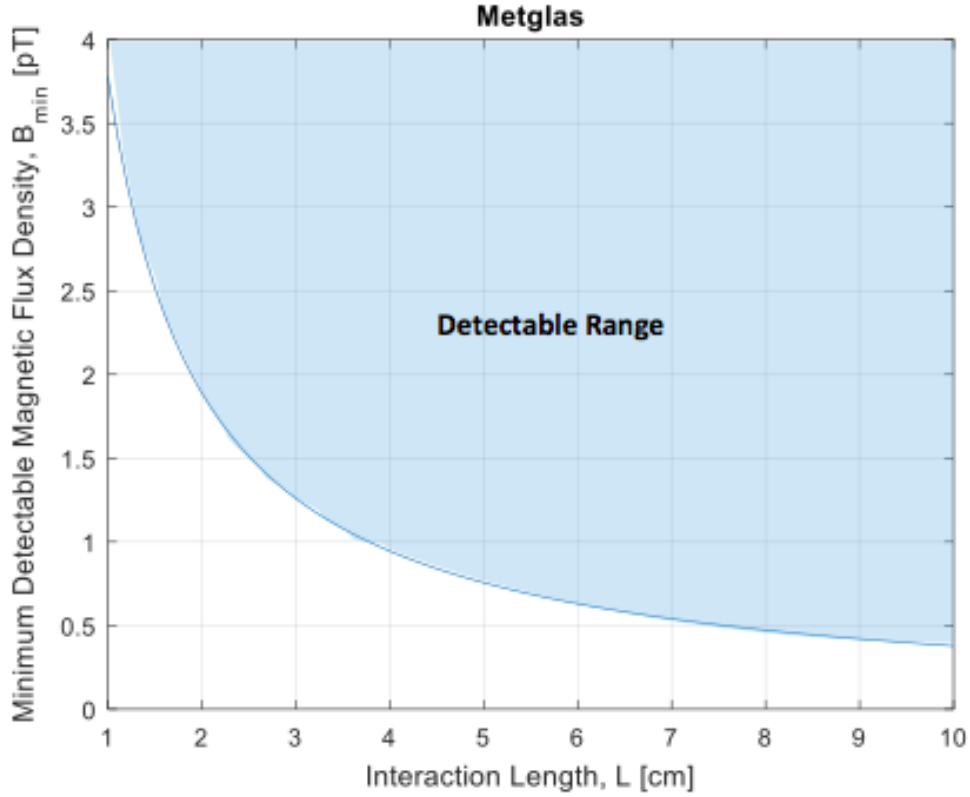


**Figure 4.2** Ultimate resolution of a magnetostrictive fiber-optic magnetic sensor with Metglas, with the parameters  $\lambda_s = 27 \text{ ppm}$ ,  $H_A = 70 \text{ A/m}$ , and  $H_{dc} = 35 \text{ A/m}$ .

#### 4.4 Terfenol-D

Terfenol-D is another magnetostrictive material and has a relatively large saturation magnetostriction value of  $\lambda_s = 1620 \text{ ppm}$ . The quantum-noise-limited magnetic flux density,  $B_{\min}$ , for Terfenol-D is plotted in Figure 4.3 as a function of the interaction length,  $L$ , of the metal coating on the fiber. Again,  $B_{\min} = \mu_o \Delta H_{\min}$ . This plot was generated using the Matlab code shown in Appendix C. Because we do not know the anisotropy field value for Terfenol-D, the value for Metglas,  $H_A = 70 \text{ A/m}$ , was used. A dc bias field of  $H_{dc} = 45 \text{ A/m}$  was selected to produce a dc strain sufficiently below the saturation magnetostriction. This value was found using the parameters ( $\epsilon = 1000 \times 10^{-6}$ )  $<$  ( $\lambda_s = 1620 \times 10^{-6}$ ). As indicated by the green

portion

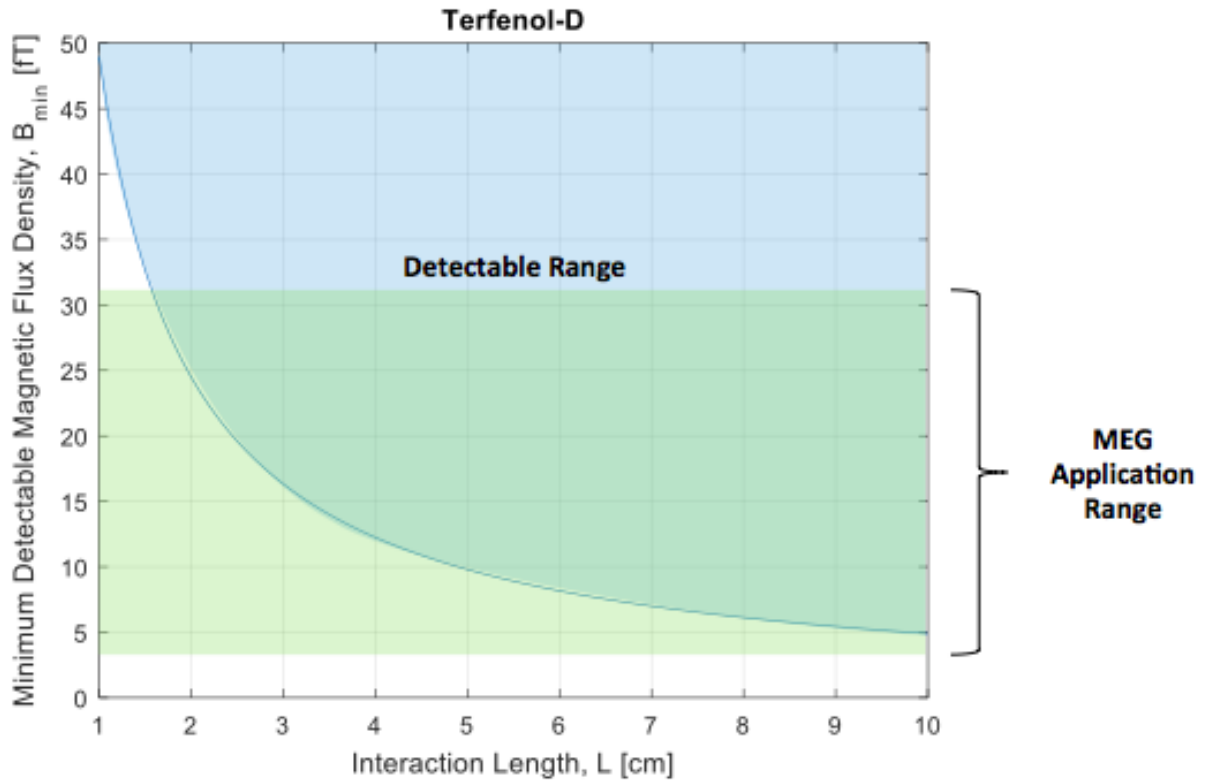


**Figure 4.3** Ultimate resolution of a magnetostrictive fiber-optic magnetic sensor with Terfenol-D, with the parameters  $\lambda_s = 1620 \text{ ppm}$ ,  $H_A = 70 \text{ A/m}$ , and  $H_{dc} = 45 \text{ A/m}$ .

of the graph, the flux density of a magnetic field sensor using Terfenol-D is within the detection range required for MEG application.

#### 4.5 Conclusion

The required detectable values of magnetic flux density of a sensor for MEG application are on the order of femtotesla. The magnetostrictive material used to coat the fiber limits the range of magnetic field values able to be detected. Sensors using Metglas can only detect flux densities on the order of picotesla, and thus cannot be used for MEG application. Using the assumptions previously stated, sensors using Terfenol-D may

provide the required detectable range, but further research into Terfenol-D's properties is required. Other magnetostrictive materials, such as those listed in section 2.3, may provide useful alternatives to Metglas and Terfenol-D. Further research into these materials is needed to determine if they are suitable materials for MEG application.

## REFERENCES

- [1] D. Cohen, "Magnetic Fields of the Human Body", *Phys. Today*, vol. 28, no. 8, p. 34, 1975.
- [2] P. Lewis and J. George, "Magnetoencephalography", *IEEE Potentials*, vol. 9, no. 4, pp. 9-13, 1990.
- [3] D. Cohen, "Biomagnetism", *AccessScience*, 2014. [Online]. Available: <http://www.accessscience.com.ezproxy.tcu.edu/content/biomagnetism/083250>. [Accessed: 18-Feb-2016].
- [4] E. Schwartz, J. Edgar, W. Gaetz and T. Roberts, "Magnetoencephalography", *Pediatr Radiol*, vol. 40, no. 1, pp. 50-58, 2009.
- [5] J. Lenz and A. Edelstein, "Magnetic sensors and their applications", *IEEE Sensors J.*, vol. 6, no. 3, pp. 631-649, 2006.
- [6] Learner.org, "Visuals: Superconducting SQUID", 2016. [Online]. Available: <https://www.learner.org/courses/physics/visual/visual.html?shortname=squid> [Accessed: 20- Feb- 2016].
- [7] What-when-how.com, "Imaging the Human Brain with Magnetoencephalography", 2016. [Online]. Available: <http://what-when-how.com/medical-informatics/imaging-the-human-brain-with-magnetoencephalography/>. [Accessed: 18- Feb- 2016].
- [8] M. Hämäläinen, R. Hari, R. Ilmoniemi, J. Knuutila and O. Lounasmaa, "Magnetoencephalography—theory, instrumentation, and applications to noninvasive studies of the working human brain", *Reviews of Modern Physics*, vol. 65, no. 2, pp. 413-497, 1993.
- [9] W. Penny and K. Friston, "Functional imaging", *Scholarpedia*, vol. 2, no. 5, p. 1478, 2007. [Online]. Available: [http://www.scholarpedia.org/article/Functional\\_imaging](http://www.scholarpedia.org/article/Functional_imaging). [Accessed: 18-Feb-2016].
- [10] F. Hyder, *Dynamic Brain Imaging*. New York, N.Y.: Humana, 2009. Pp. 167-188.
- [11] Encyclopedia Britannica, "electroencephalography", 2016. [Online]. Available: <http://www.britannica.com/science/electroencephalography/images-videos>. [Accessed: 20- Feb- 2016].
- [12] M. McClure, "Stanford psychologists uncover brain-imaging inaccuracies", *Stanford University*, 2016. [Online]. Available: <http://news.stanford.edu/news/2013/march/brain-imaging-inaccuracies-030713.html>. [Accessed: 20- Feb- 2016].

- [13] Mayfieldclinic.com, "Functional MRI and DTI", 2013. [Online]. Available: [http://www.mayfieldclinic.com/PE-fMRI\\_DTI.htm](http://www.mayfieldclinic.com/PE-fMRI_DTI.htm). [Accessed: 20- Feb- 2016].
- [14] Augustahealth.org, "PET/CT Scan", 2016. [Online]. Available: <http://www.augustahealth.org/imaging/radiology/petct-scan>. [Accessed: 20- Feb- 2016].
- [15] Chm.bris.ac.uk, "Brain Imaging", 2016. [Online]. Available: <http://www.chm.bris.ac.uk/webprojects2002/wrigglesworth/brainimaging.htm>. [Accessed: 20- Feb- 2016].
- [16] T. Sander, J. Preusser, R. Mhaskar, J. Kitching, L. Trahms and S. Knappe, "Magnetoencephalography with a chip-scale atomic magnetometer", *Biomedical Optics Express*, vol. 3, no. 5, p. 981, 2012.
- [17] S. Macintyre, *The Measurement, Instrumentation, and Sensors Handbook*. Boca Raton, Fla.: CRC Press published in cooperation with IEEE Press, 1999, p. Chapter 48.
- [18] H. Sohlström, "Fibre Optic Magnetic Field Sensors Utilizing Iron Garnet Materials", Ph.D., Royal Institute of Technology, 1993.
- [19] N. Nader-Rezvani, R. Claus and A. Sarrafzadeh, "Low-frequency Fiber Optic Magnetic Field Sensors", *Optical Engineering*, vol. 31, no. 1, pp. 23-27, 1992.
- [20] F. Bucholtz, *Fiber Optic Sensors: An Introduction for Engineers and Scientists*. Hoboken, N.J.: John Wiley & Sons, 2011, pp. 315-348.
- [21] UHV Technologies, Inc., "Advanced Electronic Material Coating on Fiber", Photonics Lab, Inc., BMDO Innovative Science and Technology Office, Contract DTRA01-99-0043, Final Rep., 1999.
- [22] J. Dillon, "Curie Temperature", *AccessScience*, 2014. [Online], Available: <http://www.accessscience.com.ezproxy.tcu.edu/content/curie-temperature/173700>. [Accessed: 30-Mar-2016].
- [23] "Nickel metal MSDS", *Sciencelab.com*, 2016. [Online]. Available: <http://www.sciencelab.com/msds.php?msdsId=9927372>. [Accessed: 30- Mar- 2016].
- [24] *Metglas*, 1st ed. Metglas, Inc., 2011. [Online]. Available: <http://www.elnamagnetics.com/wp-content/uploads/catalogs/metglas/powerlite.pdf>. [Accessed: 30- Mar- 2016].
- [25] M. Spano, K. Hathaway and H. Savage, "Magnetostriction and Magnetic Anisotropy of Field Annealed Metglas 2605 Alloys Via dc M-H loop measurements Under Stress", *J. Appl. Phys.*, vol. 53, no. 3, pp. 2667-2669, 1982.

- [26] J. Livingston, "Magnetomechanical Properties of Amorphous Metals", *Physica Status Solidi (a)*, vol. 70, no. 2, pp. 591-596, 1982.
- [27] "Terfenol-D - ETREMA Products, Inc.", *ETREMA Products, Inc.*, 2015. [Online]. Available: <http://www.etrema.com/terfenol-d/>. [Accessed: 08- Apr- 2016].
- [28] T. Kiyomiya, Y. Yamada, Y. Matsuo, H. Wakiwaka, Y. Torii and M. Makimura, "Magnetostrictive properties of Tb-Fe and Tb-Fe-Co films", *Electronics and Communications in Japan*, vol. 91, no. 5, pp. 49-55, 2008.
- [29] R. Grössinger, R. Turtelli and N. Mehmood, "Materials with high magnetostriction", *IOP Conference Series: Materials Science and Engineering*, vol. 60, p. 012002, 2014.
- [30] K. Lee, "Fiber Optic Magnetostrictive Transducers for Magnetic Field Sensing", *Optical Engineering*, vol. 34, no. 12, p. 3577, 1995.
- [31] G. Dieke and W. Watson, "Faraday Effect", *AccessScience*, 2014. [Online]. Available: <http://www.accessscience.com.ezproxy.tcu.edu/content/faraday-effect/250800>. [Accessed: 30- Mar- 2016].
- [32] "Optical Tutorials", *Thorlabs*, 2016. [Online]. Available: <https://www.thorlabs.com/tutorials.cfm?tabID=1b9018f1-1c6f-47ad-a194-f30639f7a6c5>. [Accessed: 30- Mar- 2016].
- [33] D. Cohen, "Biomagnetism", *AccessScience*, 2014. [Online]. Available: <http://www.accessscience.com.ezproxy.tcu.edu/content/biomagnetism/083250>. [Accessed: 30-Mar-2016].
- [34] L.L. Picon, V.M. Bright and E.S. Kolesar, "Detecting Low Intensity Magnetic Fields with a Magnetostrictive Fiber Optic Sensor", in *Aerospace and Electronics Conference*, NAECON, 1994, pp. 1034-1039.
- [35] T. Giallorenzi, "Fiber-optic Sensor", *AccessScience*, 2014. [Online], Available: <http://www.accessscience.com.ezproxy.tcu.edu/content/fiber-optic-sensor/255850>. [Accessed: 28:Apr-2016].
- [36] H. Gränicher, "Piezoelectricity", *AccessScience*, 2014. [Online], Available: <http://www.accessscience.com.ezproxy.tcu.edu/content/piezoelectricity/516200>. [Accessed: 28-Apr-2016].
- [37] E. Kreyszig, *Advanced Engineering Mathematics*, 4th ed. New York: John Wiley & Sons, Inc., 1979.

- [38] J. de Neufville, "Photovoltaic Effect", *AccessScience*, 2014. [Online], Available: <http://www.accessscience.com.ezproxy.tcu.edu/content/photovoltaic-effect/512110>. [Accessed: 25-Oct-2016].
- [39] T. Tayag, "Quantum-noise-limited Sensitivity of an Interferometer Using a Phase-generated Carrier Demodulation Scheme," *Optical Engineering*, vol. 41, no. 2, p. 276-277, 2002.

## APPENDIX A: MAGNETIZATION ANISOTROPY FIELD

Magnetic anisotropy refers to the dependence of magnetic properties of materials on the direction of the magnetic moments. The magnetic anisotropy field,  $H_A$ , defines an easy axis within each magnetic domain along which the magnetic moments will align when no external magnetic field is applied. The strength of a material's magnetic anisotropy field determines how easily the magnetic moments are able to move away from that easy axis. A low anisotropy field allows greater rotation, whereas a high anisotropy field results in less rotation. Each magnetostrictive material possesses its own magnetic anisotropy value.

As shown in equation 2 in Ref [A-1],  $H_A$  can be obtained using the mathematical relationship

$$\chi = \frac{M_s}{H_A} = \frac{M_s^2}{2K_u}, \quad (\text{A.1})$$

where  $\chi$  is the magnetic susceptibility,  $M_s$  is the domain magnetization per unit volume, and  $K_u$  is an anisotropy constant with units of [J/m<sup>3</sup>]. The domain magnetization,  $M_s$ , is the sum of the dipole moments making up each magnetic domain [A-2]. In magnetic materials, the individual electrons in the atoms of the material spin, creating a magnetic moment. In ferromagnetic materials, the individual electron spins are oriented together, resulting in many of the spins within a small volume aligning in the same direction in the absence of an external magnetic field. The small volume of these aligned spins is a magnetic domain. These magnetic domains are typically randomly oriented. However, in magnetostrictive materials, such as nickel, Metglas, and Terfenol-D, these domains align along the easy axis of the anisotropy field. Applying an external magnetic field

causes the domains to orient in the direction of the applied magnetic field. The ease with which the magnetic moments are able to move in response to the external magnetic field depends on the strength of that material's anisotropy field,  $H_A$ .

Equation A.1 also shows that the anisotropy field is related to the material's susceptibility,  $\chi$ . Equation 9.33 in Ref. [A-2], reproduced below, shows the relationship between this magnetic susceptibility (denoted by  $\chi_m$  below) and the material's magnetic permeability.

$$\mu = \mu_0(1 + \chi_m) \left[ \frac{H}{m} \right] \quad (A.2)$$

In this equation,  $\mu$  is the magnetic permeability of the material and  $\mu_0$  is the permeability of free space ( $\mu_0 = 4\pi \times 10^{-7} \text{ H/m}$ ). These two quantities are related according to the relationship

$$\mu = \mu_0 \mu_r, \quad (A.3)$$

where  $\mu_r$  is the relative permeability of the material. Therefore, the susceptibility and permeability are related by

$$\mu_r = 1 + \chi_m. \quad (A.4)$$

Thus, the susceptibility of a particular material can be found using its relative permeability.

Equation A.1 shows how the anisotropy field can be calculated. For the application of this research project, this anisotropy field is related to the magnetostriction of a material. The magnetostriction is given by equation 12.22 in Ref [3], reproduced below.

$$\epsilon = CH^2 \quad (A.5)$$

In this equation,  $C$  is the magnetostrictive constant for the material and  $H$  is the magnetic field to be measured. The magnetostrictive constant for the material is given by the following equation from Ref. [A-3].

$$C = \frac{3\lambda_s}{2H_A^2} \quad (\text{A.6})$$

In this equation,  $\lambda_s$  is the saturation magnetostriction. This equation shows that to obtain a large strain, the material should have a large  $\lambda_s$  and small  $H_A$ . Thus, a material with a small anisotropy field should be used.

Optimal values for the magnetostrictive constant of a material can be reached after the material has undergone a field annealing process, also known as magnetic thermal annealing. During magnetic thermal annealing, an external magnetic field is applied which reorients the easy axis in the material through a process of heating followed by cooling [A-4]. This process allows a more uniform alignment of the easy axis orientation throughout the domains in the material. In magnetostrictive materials, the orientation of the easy axis is predominantly determined by the lattice structure, shape, or internal strain of the material. The saturation magnetostriction,  $\lambda_s$ , remains relatively constant throughout the annealing process [A-3]. Figure A.1 shows a graph comparing the magnetostriction strain of a material before and after field annealing.

Anisotropic materials possess a directional dependence of their magnetic properties. The strength of the material's anisotropy field determines the ability of the magnetic moments to rotate and to align with an external magnetic field. The ease of rotation, in turn, determines the amount of magnetostrictive strain produced. To optimize

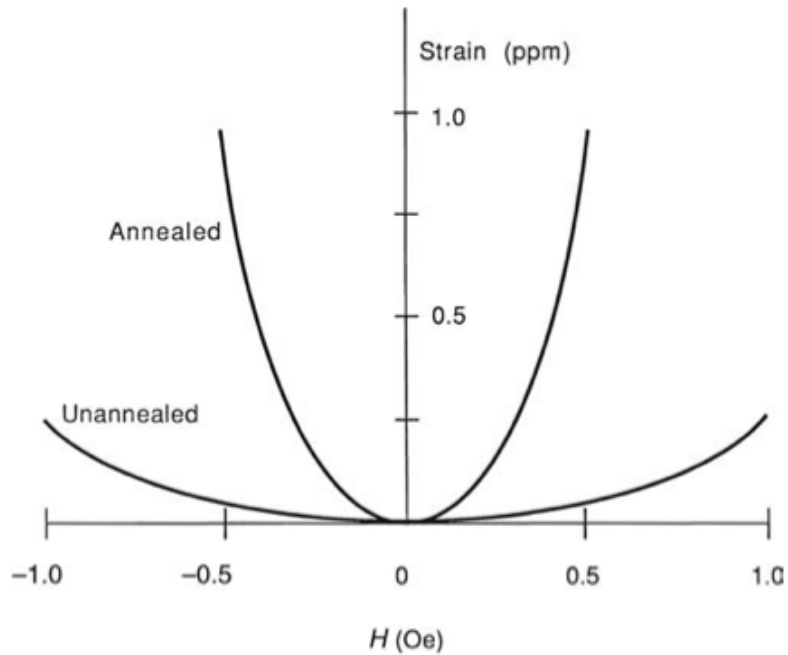


**Figure A.1** Magnetostriction of a material at low magnetic fields before and after field annealing [A-3].

the magnetostrictive effects of the material, field annealing can be used. For this application, a large strain for a small change in the magnetic field is desired, meaning the slope of the strain versus magnetic field curve, such as in Figure A.1, should be large at the operating point. Thus, a material with a small anisotropy field should be used.

## REFERENCES FOR APPENDIX A

- [A-1] J. Livingston, "Magnetomechanical Properties of Amorphous Metals", *Physica Status Solidi (a)*, vol. 70, no. 2, pp. 591-596, 1982.
- [A-2] N. Ida, *Engineering Electromagnetics*, 3rd ed. Springer: Springer International Publishing, 2015.
- [A-3] F. Bucholtz, *Fiber Optic Sensors: An Introduction for Engineers and Scientists*. Hoboken, N.J.: John Wiley & Sons, 2011, pp. 315-348.
- [A-4] "Magnetic Thermal Annealing: An Effective Process To Enhance The Performance Of Magnetic Devices And Materials", *Micro Magnetics*. [Online]. Available: <http://www.directvacuum.com/pdf/anneal.pdf>. [Accessed: 06- Dec- 2016].

## APPENDIX B: PROGRAM FOR METGLAS

```
% Magnetic_Sensor_Resolution_v1.m: This program plots the
% quantum-noise-limited resolution of an interferometric sensor based on a
% PGC demodulation scheme for Metglas. The transducer in the sensing arm of the
% interferometer is a magnetostrictive film.
%
% References:
% T. J. Tayag, Opt. Eng., vol. 41, no. 2, pp. 276-277 (Feb 2002).
% F. Bucholtz, Fiber Optics Sensors: An Introduction for Engineers and
% Scientists, E. Udd and W. Spillman (eds.), chap. 12, Wiley, 2011.
%
% Author: T. J. Tayag, L. E. Getz
% Date: 29 September 2016
% Last revision: 25 January 2017
```

```
clear all;
```

```
% Define variables
```

```
P_i = 10e-3;    % laser power (W)
eta = 0.45;    % photodetector quantum efficiency (%)
h = 6.62617e-34; % Planck's constant (J.s)
c = 299792458; % speed of light in vacuum (m/s)
lambda = 850e-9; % wavelength of light (m)
nu = c/lambda; % light frequency (Hz)
del_nu = 100; % detection electronics bandwidth (Hz)
k_o = 2*pi/lambda; % free space propagation constant (1/m)
Delta = lambda/4; % quiescent path length difference (radians)
```

```
% Define the SNR = 1
```

```
term1 = sqrt(P_i*eta/(h*nu*del_nu));
term2 = 1-besselj(0,2*pi)*cos(4*k_o*Delta);
term3 = 2+2*besselj(0,pi)*cos(2*k_o*Delta);
term4 = besselj(0,pi)*sin(2*k_o*Delta);
```

```
% Use this displacement value to solve for B_min, the minimum detectable
% magnetic flux density.
```

```
% Define variables
```

```
n = 1.46;    % index of fiber core
eta2 = 0.9; % strain transfer efficiency (%)
lambda = 850e-9; % wavelength of light (m)
zeta = 0.78; % strain optic correction factor
```

```
% Define variables for Metglas
```

```

lambda_s = 27e-6; % saturation magnetostriction of material (m)
H_A = 70; % anisotropy field of material (A/m)
mu_0 = pi*4e-7; % permeability of free space (H/m)
mu_r = 600000; % maximum dc permeability annealed for Metglas alloys
C = 3*lambda_s/(2*H_A^2); % magnetostrictive constant

phi = (2*pi*n/lambda)*zeta*eta2*C;

% Plot B_min vs L for small L
H_dc = 35; % dc bias field (A/m)

syms deltaH; % creates the symbolic variable deltaH

output = zeros(90,2);
counter = 0;
for L = 1e-2:1e-3:0.1
    counter = counter+1;
    eqn = 1 == term1.*L.*phi.*(2.*H_dc).*deltaH.*sqrt(term2./(term3-
4.*L.*phi.*(2.*H_dc).*deltaH.*term4));
    H = solve(eqn, deltaH);
    B_min = mu_0*H;
    output(counter,:) = [L B_min];
end

figure
plot(output(:,1)*1e2,output(:,2)*1e12);
xlabel('Interaction Length, L [cm]');
ylabel('Minimum Detectable Magnetic Flux Density, B_m_i_n [pT]');
title('Metglas');
grid on

```

## APPENDIX C: PROGRAM FOR TERFENOL-D

```
% Magnetic_Sensor_Resolution_v1.m: This program plots the
% quantum-noise-limited resolution of an interferometric sensor based on a
% PGC demodulation scheme for Terfenol-D. The transducer in the sensing arm of the
% interferometer is a magnetostrictive film.
%
% References:
% T. J. Tayag, Opt. Eng., vol. 41, no. 2, pp. 276-277 (Feb 2002).
% F. Bucholtz, Fiber Optics Sensors: An Introduction for Engineers and
% Scientists, E. Udd and W. Spillman (eds.), chap. 12, Wiley, 2011.
%
% Author: T. J. Tayag, L. E. Getz
% Date: 29 September 2016
% Last revision: 25 January 2017
```

```
clear all;
```

```
% Define variables
```

```
P_i = 10e-3;    % laser power (W)
eta = 0.45;    % photodetector quantum efficiency (%)
h = 6.62617e-34; % Planck's constant (J.s)
c = 299792458; % speed of light in vacuum (m/s)
lambda = 850e-9; % wavelength of light (m)
nu = c/lambda; % light frequency (Hz)
del_nu = 100; % detection electronics bandwidth (Hz)
k_o = 2*pi/lambda; % free space propagation constant (1/m)
Delta = lambda/4; % quiescent path length difference (radians)
```

```
% Define the SNR = 1
```

```
term1 = sqrt(P_i*eta/(h*nu*del_nu));
term2 = 1-besselj(0,2*pi)*cos(4*k_o*Delta);
term3 = 2+2*besselj(0,pi)*cos(2*k_o*Delta);
term4 = besselj(0,pi)*sin(2*k_o*Delta);
```

```
% Use this displacement value to solve for B_min, the minimum detectable
% magnetic flux density.
```

```
% Define variables
```

```
n = 1.46;    % index of fiber core
eta2 = 0.9; % strain transfer efficiency (%)
lambda = 850e-9; % wavelength of light (m)
zeta = 0.78; % strain optic correction factor
```

```
% Define variables for Metglas
```

```

lambda_s = 1620e-6; % saturation magnetostriction of material (m)
H_A = 70; % anisotropy field of material (A/m)
mu_0 = pi*4e-7; % permeability of free space (H/m)
C = 3*lambda_s/(2*H_A^2); % magnetostrictive constant

phi = (2*pi*n/lambda)*zeta*eta2*C;

% Plot B_min vs L for small L
H_dc = 45; % dc bias field (A/m)

syms deltaH; % creates the symbolic variable deltaH

output = zeros(90,2);
counter = 0;
for L = 1e-2:1e-3:0.1
    counter = counter+1;
    eqn = 1 == term1.*L.*phi.*(2.*H_dc).*deltaH.*sqrt(term2./(term3-
4.*L.*phi.*(2.*H_dc).*deltaH.*term4));
    H = solve(eqn, deltaH);
    B_min = mu_0*H;
    output(counter,:) = [L B_min];
end

figure
plot(output(:,1)*1e2,output(:,2)*1e15);
xlabel('Interaction Length, L [cm]');
ylabel('Minimum Detectable Magnetic Flux Density, B_m_i_n [fT]');
title('Terfenol-D');
grid on

```